

A unified model for reverberation and submerged object scattering in a stratified ocean waveguide

Nicholas C. Makris and Purnima Ratilal

Department of Ocean Engineering, Massachusetts Institute of Technology, Cambridge, Massachusetts 02139

(Received 24 March 2000; revised 14 September 2000; accepted 13 November 2000)

A unified model for reverberation and submerged target scattering in a stratified medium is developed from wave theory. The advantage of the unified approach is that it enables quantitative predictions to be made of the target-echo-to-reverberation ratio in an ocean waveguide. Analytic expressions are derived for both deterministic and stochastic scattering from the seafloor and subseafloor. Asymptotic techniques are used to derive expressions for the scattering of broadband waveforms from distant objects or surfaces. Expressions are then obtained for the scattered field after beamforming with a horizontal line array. The model is applied to problems of active detection in shallow water. Sample calculations for narrow-band signals indicate that the detection of submerged target echoes above diffuse seafloor reverberation is highly dependent upon water column and sediment stratification as well as array aperture, source, receiver, and target locations, in addition to the scattering properties of the target and seafloor. The model is also applied to determine the conditions necessary for echo returns from discrete geomorphologic features of the seafloor and subseafloor to stand prominently above diffuse seafloor reverberation. This has great relevance to the geologic clutter problem encountered by active sonar systems operating in shallow water, as well as to the remote sensing of underwater geomorphology. © 2001 Acoustical Society of America. [DOI: 10.1121/1.1339826]

PACS numbers: 43.30.Gv, 43.30.Hw, 43.30.Vh [DLB]

I. INTRODUCTION

A common problem in the active detection and localization of a radar or sonar target arises when scattered returns from the target become indistinguishable from returns from randomly rough boundaries, volume inhomogeneities, or deterministic features of the environment. The goal of the present article is to investigate the extent to which environmental reverberation limits the ability to detect and localize a target submerged in an ocean waveguide, where methods developed for the radar half-space problem are inapplicable due to the added complications of multi-modal propagation and dispersion.

To this end, a unified model for 3-D reverberation and submerged target scattering in a stratified medium is developed from wave theory. The model is fully *bistatic* and stems directly from Green's theorem, since it generalizes Ingenito's approach^{1,2} for harmonic scattering in a stratified medium by incorporating stochastic scatterers and time-dependent sources. While it is consistent with certain narrow-band results of previous "heuristic" derivations³⁻⁷ for shallow water reverberation measured with an omni-directional receiver that are based on the work of Bucker and Morris,⁴ it offers more insight and generality since it is developed from first principles with explicitly stated assumptions. For example, it clearly obeys reciprocity for source-receiver locations within a layered media, which is important in properly modeling the absolute level of returns from targets or surfaces within the seafloor, and it allows absolute comparison between reverberation and deterministic target returns. Such comparison led to inconsistencies in previous formulations as noted in Ref. 3. It also provides analytic expressions for the three-dimensional (3-D) field scattered bistatically by

both stochastic and deterministic objects from a source with arbitrary time function, as well as the associated spatial and temporal covariances. This enables realistic modeling of the moments of the raw reverberant field received over extended spatial and temporal apertures as well as the output after subsequent processing with standard beamforming and broadband signal processing techniques. In the present article, applications of the theory are restricted to systems which employ the beamforming and temporally incoherent processing widely used in narrow-band signal reception. Analytic expressions for the statistical moments of the scattered field are obtained directly, but can also be obtained by sample averaging over realizations by Monte Carlo simulations, as for example is done for rough surface scattering in Ref. 8. The relative merit of either approach depends on the relative difficulty in evaluating the analytically obtained moments or performing the Monte Carlo simulations for the given problem. The analytic approach has proven to be more advantageous and insightful for the illustrative examples of the present article.

The primary motivation for developing the unified model is to compare the absolute level of target echo returns with those from the seafloor and to investigate how these vary in both absolute and relative level as a function of water column and sediment stratification, receiving array aperture, and source, receiver, and target locations in a shallow water waveguide. Another major focus of the present article is to investigate the manner in which scattering from both extended geomorphologic features and randomly rough patches of the seafloor and subseafloor contribute to measured reverberation. The latter typically makes up the diffuse reverberant background, which has an expected intensity that decays

in time after the arrival of the direct signal waveform. The former typically leads to geological clutter, which is defined as any set of acoustic returns from the seabed that stand significantly above the diffuse and temporally decaying reverberation background. Geological clutter is a primary problem in active sonar operations in shallow water. This is because the clutter can be confused with or camouflage returns intended from a submerged target.

A goal of this work is then to determine plausible physical mechanisms for geological clutter by use of the unified model. To do so, both first-order perturbation theory and empirical Lambert–Mackenzie⁹ models are used to describe stochastic scattering from a randomly rough seafloor. These models, together with deterministic models for scattering from seafloor features, are used to determine scenarios where geologic clutter is significant. The present focus is on seafloor features with mean surfaces that are finite and inclined with the reflection properties of the layer to which they belong, since such features are ubiquitous in continental shelf waters. While a large literature exists for scattering from 2-D features in a waveguide, the focus of the present work is on scattering from 3-D features in a waveguide. Apparently, the only previous work on deterministic scattering from 3-D seafloor features in a waveguide has been for acoustically compact ($ka \ll 1$) protrusions on perfectly reflecting bottoms,¹⁰ but compact targets are too weak to comprise geological clutter in a long-range active sonar system and are not relevant to the present analysis. A review of the general literature on 3-D scattering in an ocean waveguide is given in Ref. 11. All illustrative examples in the present article employ time-windowed cw source waveforms and monostatic geometries to investigate the central detection issues with as simple an approach as possible.

II. THE UNIFIED MODEL

A. The single-scatter approximation for 3-D scattering from an object of arbitrary shape in a layered medium

A number of simplifying conditions¹¹ that apply to a wide variety of active sonar problems in the ocean enable the field scattered from an object submerged in a stratified medium to be approximated, from Green's exact theorem, as a linear function of the object's plane wave scatter function.¹² The plane wave scatter function $S(\theta, \phi; \theta_i, \phi_i)$ at frequency f is defined in Appendix A, where its relationship to Green's theorem and the traditional target strength and scattering strength measures of ocean acoustics is explained.

To formulate the unified model, it is convenient to initially follow Refs. 1, 2, and 11 by placing the object centroid at the center of all coordinate systems. The source coordinates are then defined by (x_0, y_0, z_0) , receiver coordinates by (x, y, z) , and coordinates on the surface of the object by (x_t, y_t, z_t) where the positive z axis points downward and normal to the interfaces between horizontal strata. Spatial cylindrical (ρ, θ, z) and spherical systems (r, θ, ϕ) are defined by $x = r \sin \theta \cos \phi$, $y = r \sin \theta \sin \phi$, $z = r \cos \theta$, and $\rho^2 = x^2 + y^2$. The horizontal and vertical wave number components for the n th mode are respectively $\xi_n = k \sin \alpha_n$ and

$\gamma_n = k \cos \alpha_n$, where $k^2 = \xi_n^2 + \gamma_n^2$ and the wave number magnitude k equals the angular frequency ω divided by the sound speed c in the target layer.

The spectral component of the scattered field for a time-harmonic source of frequency f at \mathbf{r}_0 and a receiver at \mathbf{r} then becomes

$$\Phi_s(\mathbf{r}|\mathbf{r}_0) \approx \sum_{m=1}^{\infty} \sum_{n=1}^{\infty} \Phi_s^{(m,n)}(\mathbf{r}|\mathbf{r}_0), \quad (1a)$$

where

$$\begin{aligned} \Phi_s^{(m,n)}(\mathbf{r}|\mathbf{r}_0) = & \frac{4\pi}{k} [A_m(\mathbf{r})A_n(\mathbf{r}_0)S(\pi - \alpha_m, \phi; \alpha_n, \phi_0 + \pi) \\ & - B_m(\mathbf{r})A_n(\mathbf{r}_0)S(\alpha_m, \phi; \alpha_n, \phi_0 + \pi) \\ & - A_m(\mathbf{r})B_n(\mathbf{r}_0)S(\pi - \alpha_m, \phi; \pi - \alpha_n, \phi_0 + \pi) \\ & + B_m(\mathbf{r})B_n(\mathbf{r}_0)S(\alpha_m, \phi; \pi - \alpha_n, \phi_0 + \pi)], \end{aligned} \quad (1b)$$

and

$$A_m(\mathbf{r}) = \frac{i}{d(0)} (8\pi\xi_m\rho)^{-1/2} u_m(z) N_m^- e^{i(\xi_m\rho + \gamma_m D - \pi/4)}, \quad (2a)$$

$$B_m(\mathbf{r}) = \frac{i}{d(0)} (8\pi\xi_m\rho)^{-1/2} u_m(z) N_m^+ e^{i(\xi_m\rho - \gamma_m D - \pi/4)}, \quad (2b)$$

$$A_n(\mathbf{r}_0) = \frac{i}{d(z_0)} (8\pi\xi_n\rho_0)^{-1/2} u_n(z_0) N_n^- e^{i(\xi_n\rho_0 + \gamma_n D - \pi/4)}, \quad (2c)$$

$$B_n(\mathbf{r}_0) = \frac{i}{d(z_0)} (8\pi\xi_n\rho_0)^{-1/2} u_n(z_0) N_n^+ e^{i(\xi_n\rho_0 - \gamma_n D - \pi/4)}, \quad (2d)$$

are the down- and up-going plane wave amplitudes in the layer of the object, D is the depth of the object center from the sea surface, $d(z)$ is the density at depth z , and $u_n(z)$ are the mode functions. The product of $e^{-i2\pi ft}$ and the right-hand side of Eq. (1a) yields the time-harmonic scattered field. The mode functions are normalized¹³ according to

$$\delta_{nm} = \int_{-D}^{\infty} \frac{u_m^*(z)u_n(z)}{d(z)} dz, \quad (3)$$

and must be decomposable into up- and down-going plane waves via

$$u_n(z) = N_n^- e^{i\gamma_n(z+D)} - N_n^+ e^{-i\gamma_n(z+D)} \quad (4)$$

in the layer of the object, where N_n^- and N_n^+ are the amplitudes of down- and up-going plane waves in this layer. In a Pekeris waveguide, for example,

$$N_n^- = N_n^+ = \frac{\sqrt{2}}{2i} \left[\frac{1}{d} \left(H - \frac{\sin 2\gamma_n H}{2\gamma_n} \right) + \frac{1}{d_b} \frac{\sin^2 \gamma_n H}{\sqrt{\xi_n^2 - (\omega/c_b)^2}} \right]^{-1/2}, \quad (5)$$

where d_b and c_b are the density and sound speed of the bottom. If the mode functions are specified at any two depths, z_1 and z_2 within the target layer, the down- and up-going plane wave amplitudes can be readily obtained as

$$\begin{bmatrix} N_n^- \\ -N_n^+ \end{bmatrix} = \begin{bmatrix} e^{i\gamma_n(z_1+D)} & e^{-i\gamma_n(z_1+D)} \\ e^{i\gamma_n(z_2+D)} & e^{-i\gamma_n(z_2+D)} \end{bmatrix}^{-1} \begin{bmatrix} u_n(z_1) \\ u_n(z_2) \end{bmatrix}. \quad (6)$$

Equations (1)–(6) for the scattered field from an arbitrarily shaped object in a waveguide differ from Ingenito's formulation¹ in a number of ways. The most substantial difference is that, by inclusion of Eqs. (4) and (6), they explicitly show how the scattered field for an arbitrarily shaped object can be computed in a stratified medium. Ingenito also defines the plane wave scatter function differently than most standard texts by describing the incident plane wave in terms of *the direction it comes from* rather than *the direction it goes to*. The latter, standard approach, is adopted here.

Finally, the more standard mode function normalization of Ref. 13 is adopted here, so that Eq. (1) obeys reciprocity as defined in Appendix A2 of Ref. 13, so that $d(z_0)\Phi_s(\mathbf{r}|\mathbf{r}_0) = d(z)\Phi_s(\mathbf{r}_0|\mathbf{r})$. Satisfaction of reciprocity becomes important for an approach if it is to yield accurate estimates of the scattered field when the source, receiver, and target are in layers that have significantly different densities, and is a natural consequence of the use of Green's theorem in the present formulation, but has been left unaddressed as an issue in previous heuristic reverberation formulations.^{3–7} The issue becomes of practical concern in modeling the level of returns from targets or surfaces buried in the seafloor from sonar systems operating in the water column above.

A more general expression than Eqs. (1)–(6), for the scattered field from an arbitrarily shaped object in a stratified medium, is given in Refs. 2 and 11 in terms of wave number integrals. As noted in Ref. 11, the more general wave num-

ber formulation is valid when (1) the propagation medium is horizontally stratified and range independent; (2) the object is contained within an iso-velocity layer; (3) multiple reflections between the *object* and waveguide boundaries make a negligible contribution at the receiver; and (4) the range from the object to source or receiver is large enough that the scattered field can be expressed as a linear function of the object's plane wave scatter function. All of these conditions then must be satisfied for Eqs. (1)–(6) to be valid, with one additional constraint. The ranges involved must be large enough that the Green's functions, from source-to-target and target-to-receiver, are accurately approximated as sums of discrete modes. The latter is an expected consequence of the Riemann–Lebesgue lemma.¹⁴ The present formulation and its spectral equivalent have been implemented for target scattering in a waveguide over the full 360-degree span of bistatic angles in Refs. 1, 2 and 11. It is noteworthy that this formulation includes the scattering of evanescent waves by analytic continuation of the scatter function, as has been previously discussed and implemented in Refs. 2 and 11, as well as in Ref. 8 which uses a formulation similar to Ingenito's.

B. The field scattered from general stochastic targets

By allowing the scatter function for the object to be a random variable, the single-scatter formulation of the previous section applies to the more general problem of scattering from a stochastic target submerged in a waveguide. This approach is particularly valuable in modeling scattering from targets of unknown shape or orientation, randomly rough surface interfaces, or stochastic volume heterogeneities, all of which can contribute significantly to the reverberant field measured in shallow water.

The moments of the scattered field can be derived analytically to determine its expected behavior. The mean field, for example, becomes

$$\langle \Phi_s(\mathbf{r}|\mathbf{r}_0) \rangle \approx \sum_{m=1}^{\infty} \sum_{n=1}^{\infty} \langle \Phi_s^{(m,n)}(\mathbf{r}|\mathbf{r}_0) \rangle, \quad (7)$$

where

$$\begin{aligned} \langle \Phi_s^{(m,n)}(\mathbf{r}|\mathbf{r}_0) \rangle &= \frac{4\pi}{k} [A_m(\mathbf{r})A_n(\mathbf{r}_0)\langle S(\pi - \alpha_m, \phi; \alpha_n, \phi_0 + \pi) \rangle - B_m(\mathbf{r})A_n(\mathbf{r}_0)\langle S(\alpha_m, \phi; \alpha_n, \phi_0 + \pi) \rangle \\ &\quad - A_m(\mathbf{r})B_n(\mathbf{r}_0)\langle S(\pi - \alpha_m, \phi; \pi - \alpha_n, \phi_0 + \pi) \rangle + B_m(\mathbf{r})B_n(\mathbf{r}_0)\langle S(\alpha_m, \phi; \pi - \alpha_n, \phi_0 + \pi) \rangle] \end{aligned} \quad (8)$$

while the mutual intensity of the field scattered for receivers at \mathbf{r} and \mathbf{r}' becomes

$$\langle \Phi_s(\mathbf{r}|\mathbf{r}_0)\Phi_s^*(\mathbf{r}'|\mathbf{r}_0) \rangle \approx \sum_{m=1}^{\infty} \sum_{n=1}^{\infty} \sum_{m'=1}^{\infty} \sum_{n'=1}^{\infty} \langle \Phi_s^{(m,n)}(\mathbf{r}|\mathbf{r}_0)\Phi_s^{(m',n')}(\mathbf{r}'|\mathbf{r}_0) \rangle, \quad (9)$$

where

$$\begin{aligned} \langle \Phi_s^{(m,n)}(\mathbf{r}|\mathbf{r}_0)\Phi_s^{(m',n')}(\mathbf{r}'|\mathbf{r}_0) \rangle &= \left(\frac{4\pi}{k} \right)^2 [A_m(\mathbf{r})A_n(\mathbf{r}_0)A_{m'}^*(\mathbf{r}')A_{n'}^*(\mathbf{r}_0)\langle S(\pi - \alpha_m, \phi; \alpha_n, \phi_0 + \pi)S^*(\pi - \alpha_{m'}, \phi'; \alpha_{n'}, \phi_0 + \pi) \rangle \\ &\quad - A_m(\mathbf{r})A_n(\mathbf{r}_0)B_{m'}^*(\mathbf{r}')A_{n'}^*(\mathbf{r}_0)\langle S(\pi - \alpha_m, \phi; \alpha_n, \phi_0 + \pi)S^*(\alpha_{m'}, \phi'; \alpha_{n'}, \phi_0 + \pi) \rangle \\ &\quad - A_m(\mathbf{r})A_n(\mathbf{r}_0)A_{m'}^*(\mathbf{r}')B_{n'}^*(\mathbf{r}_0)\langle S(\pi - \alpha_m, \phi; \alpha_n, \phi_0 + \pi)S^*(\pi - \alpha_{m'}, \phi'; \pi - \alpha_{n'}, \phi_0 + \pi) \rangle \\ &\quad - A_m(\mathbf{r})A_n(\mathbf{r}_0)B_{m'}^*(\mathbf{r}')B_{n'}^*(\mathbf{r}_0)\langle S(\alpha_m, \phi; \alpha_n, \phi_0 + \pi)S^*(\alpha_{m'}, \phi'; \pi - \alpha_{n'}, \phi_0 + \pi) \rangle] \end{aligned}$$

$$\begin{aligned}
& + A_m(\mathbf{r})A_n(\mathbf{r}_0)B_m^*(\mathbf{r}')B_n^*(\mathbf{r}_0)\langle S(\pi-\alpha_m, \phi; \alpha_n, \phi_0+\pi)S^*(\alpha_{m'}, \phi'; \pi-\alpha_{n'}, \phi_0+\pi)\rangle \\
& - B_m(\mathbf{r})A_n(\mathbf{r}_0)A_m^*(\mathbf{r}')A_n^*(\mathbf{r}_0)\langle S(\alpha_m, \phi; \alpha_n, \phi_0+\pi)S^*(\pi-\alpha_{m'}, \phi'; \alpha_{n'}, \phi_0+\pi)\rangle \\
& + B_m(\mathbf{r})A_n(\mathbf{r}_0)B_m^*(\mathbf{r}')A_n^*(\mathbf{r}_0)\langle S(\alpha_m, \phi; \alpha_n, \phi_0+\pi)S^*(\alpha_{m'}, \phi'; \alpha_{n'}, \phi_0+\pi)\rangle \\
& + B_m(\mathbf{r})A_n(\mathbf{r}_0)A_m^*(\mathbf{r}')B_n^*(\mathbf{r}_0)\langle S(\alpha_m, \phi; \alpha_n, \phi_0+\pi)S^*(\pi-\alpha_{m'}, \phi'; \pi-\alpha_{n'}, \phi_0+\pi)\rangle \\
& - B_m(\mathbf{r})A_n(\mathbf{r}_0)B_m^*(\mathbf{r}')B_n^*(\mathbf{r}_0)\langle S(\alpha_m, \phi; \alpha_n, \phi_0+\pi)S^*(\alpha_{m'}, \phi'; \pi-\alpha_{n'}, \phi_0+\pi)\rangle \\
& - A_m(\mathbf{r})B_n(\mathbf{r}_0)A_m^*(\mathbf{r}')A_n^*(\mathbf{r}_0)\langle S(\pi-\alpha_m, \phi; \pi-\alpha_n, \phi_0+\pi)S^*(\pi-\alpha_{m'}, \phi'; \alpha_{n'}, \phi_0+\pi)\rangle \\
& + A_m(\mathbf{r})B_n(\mathbf{r}_0)B_m^*(\mathbf{r}')A_n^*(\mathbf{r}_0)\langle S(\pi-\alpha_m, \phi; \pi-\alpha_n, \phi_0+\pi)S^*(\alpha_{m'}, \phi'; \alpha_{n'}, \phi_0+\pi)\rangle \\
& + A_m(\mathbf{r})B_n(\mathbf{r}_0)A_m^*(\mathbf{r}')B_n^*(\mathbf{r}_0)\langle S(\pi-\alpha_m, \phi; \pi-\alpha_n, \phi_0+\pi)S^*(\pi-\alpha_{m'}, \phi'; \pi-\alpha_{n'}, \phi_0+\pi)\rangle \\
& - A_m(\mathbf{r})B_n(\mathbf{r}_0)B_m^*(\mathbf{r}')B_n^*(\mathbf{r}_0)\langle S(\pi-\alpha_m, \phi; \pi-\alpha_n, \phi_0+\pi)S^*(\alpha_{m'}, \phi'; \pi-\alpha_{n'}, \phi_0+\pi)\rangle \\
& + B_m(\mathbf{r})B_n(\mathbf{r}_0)A_m^*(\mathbf{r}')A_n^*(\mathbf{r}_0)\langle S(\alpha_m, \phi; \pi-\alpha_n, \phi_0+\pi)S^*(\pi-\alpha_{m'}, \phi'; \alpha_{n'}, \phi_0+\pi)\rangle \\
& - B_m(\mathbf{r})B_n(\mathbf{r}_0)B_m^*(\mathbf{r}')A_n^*(\mathbf{r}_0)\langle S(\alpha_m, \phi; \pi-\alpha_n, \phi_0+\pi)S^*(\alpha_{m'}, \phi'; \alpha_{n'}, \phi_0+\pi)\rangle \\
& - B_m(\mathbf{r})B_n(\mathbf{r}_0)A_m^*(\mathbf{r}')B_n^*(\mathbf{r}_0)\langle S(\alpha_m, \phi; \pi-\alpha_n, \phi_0+\pi)S^*(\pi-\alpha_{m'}, \phi'; \pi-\alpha_{n'}, \phi_0+\pi)\rangle \\
& + B_m(\mathbf{r})B_n(\mathbf{r}_0)B_m^*(\mathbf{r}')B_n^*(\mathbf{r}_0)\langle S(\alpha_m, \phi; \pi-\alpha_n, \phi_0+\pi)S^*(\alpha_{m'}, \phi'; \pi-\alpha_{n'}, \phi_0+\pi)\rangle].
\end{aligned} \tag{10}$$

The spatial covariance, or cross spectral density, of the scattered field,

$$\begin{aligned}
& \langle \Phi_s(\mathbf{r}|\mathbf{r}_0)\Phi_s^*(\mathbf{r}'|\mathbf{r}_0) \rangle - \langle \Phi_s(\mathbf{r}|\mathbf{r}_0) \rangle \langle \Phi_s^*(\mathbf{r}'|\mathbf{r}_0) \rangle \\
& \approx \sum_{m=1}^{\infty} \sum_{n=1}^{\infty} \sum_{m'=1}^{\infty} \sum_{n'=1}^{\infty} \langle \Phi_s^{(m,n)}(\mathbf{r}|\mathbf{r}_0)\Phi_s^{(m',n')*}(\mathbf{r}'|\mathbf{r}_0) \rangle \\
& \quad - \langle \Phi_s^{(m,n)}(\mathbf{r}|\mathbf{r}_0) \rangle \langle \Phi_s^{(m',n')*}(\mathbf{r}'|\mathbf{r}_0) \rangle,
\end{aligned} \tag{11}$$

follows directly from Eqs. (7)–(10), and has been implemented for fluctuating targets submerged in an ocean waveguide.¹⁵

C. When scattering statistically decorrelates the waveguide modes

Many useful scattering properties of a random target are described by the covariance of its scatter function, which couples incident modes with n and n' subscripts together with scattered modes with m and m' subscripts in the cross spectral density of Eq. (11). Under many situations of practical interest in the scattering from fluctuating targets or randomly rough surfaces, the n and n' incident modes decouple as do the scattered m and m' modes.

Assume that the random target's characteristic dimension L is large compared to the wavelength λ and that for any realization it has complicated structure with significant variations on the wavelength scale. These assumptions are used extensively in radar to describe fluctuating targets,^{16,17} such as aircraft of unknown shape and orientation, and in radar, statistical optics, and acoustics to describe scattering from randomly rough surfaces.^{18–20} They typically lead to circular complex Gaussian random (CCGR) fluctuations in the scattered field over different statistical realizations of the

target.^{16–21} When the target is a randomly rough surface, these assumptions are equivalent to restricting the correlation length of the surface roughness to be much smaller than the dimension L of the targeted surface. In this case the scattered field is usually termed *diffuse* or *incoherent* “because of its wide angular spread and lack of phase relationship with the incident wave.”¹⁸

For any realization of such a random surface or target, say for example the k th realization, its scatter function $S_k(\Omega; \Omega_i)$ will be highly oscillatory in magnitude and phase over both incident $\Omega_i = (\theta_i, \phi_i)$ and scattered $\Omega = (\theta, \phi)$ directions and will have a complicated lobe pattern. This lobe pattern will vary significantly over random realizations of the surface or target due to changes in constructive and destructive interference, making the scatter function representing all realizations $S(\Omega; \Omega_i)$ a random variable with zero expected value, $\langle S(\Omega; \Omega_i) \rangle = 0$. Due to the complicated structure of the target, the angular width of any lobe in the scatter function will be on the order of the minimum width set by diffraction of λ/L , which is small by assumption. The second moment of the scatter function $\langle S(\Omega; \Omega_i)S^*(\Omega'; \Omega'_i) \rangle$ for incident angles Ω_i, Ω'_i and scattered angles Ω, Ω' can be thought of as an ensemble average of $S_k(\Omega; \Omega_i)S_k^*(\Omega'; \Omega'_i)$ over realizations of the random surface. This product will oscillate about zero across realizations k for $|\Omega_i - \Omega'_i| > \lambda/L$ and $|\Omega - \Omega'| > \lambda/L$ so that the ensemble average will tend to zero due to term by term cancellation. Here λ/L behaves as an angular correlation width of the scatter function over variations in both incident and scattered angle. The product will tend to become positive definite for $|\Omega_i - \Omega'_i| \leq \lambda/L, |\Omega - \Omega'| \leq \lambda/L$, however, so that the ensemble average will approach $\langle |S(\Omega; \Omega_i)|^2 \rangle$.

Applying this reasoning to stochastic targets or surface

patches in a waveguide, the covariance of the scatter function can be written as

$$\begin{aligned} & \langle S(\alpha_m, \phi; \alpha_n, \phi_0 + \pi) S^*(\alpha_{m'}, \phi'; \alpha_{n'}, \phi_0 + \pi) \rangle - \langle S(\alpha_m, \phi; \alpha_n, \phi_0 + \pi) \rangle \langle S^*(\alpha_{m'}, \phi'; \alpha_{n'}, \phi_0 + \pi) \rangle \\ & = \delta_{nn'} \delta_{mm'} C_{mn}(\mathbf{r}, \mathbf{r}' | \mathbf{r}_0), \end{aligned} \quad (12a)$$

where

$$C_{mn}(\mathbf{r}, \mathbf{r}' | \mathbf{r}_0) = \langle S(\alpha_m, \phi; \alpha_n, \phi_0 + \pi) S^*(\alpha_m, \phi'; \alpha_n, \phi_0 + \pi) \rangle - \langle S(\alpha_m, \phi; \alpha_n, \phi_0 + \pi) \rangle \langle S^*(\alpha_m, \phi'; \alpha_n, \phi_0 + \pi) \rangle, \quad (12b)$$

when the angular separation $|\alpha_n - \alpha_{n'}|$ between modes n and n' is greater than the angular correlation width λ/L set by diffraction. In practical scenarios, this criterion will apply most stringently to the dominant modes, where full decorrelation will occur for $|\alpha_{n+1} - \alpha_n|$ on the order or greater than λ/L . For trapped modes, $|\alpha_{n+1} - \alpha_n|$ is less than the critical angle of the bottom.

Insertion of Eq. (12a) into Eq. (11) then leads to a great simplification in the spatial covariance of the scattered field

$$\begin{aligned} & \langle \Phi_s(\mathbf{r} | \mathbf{r}_0) \Phi_s^*(\mathbf{r}' | \mathbf{r}_0) \rangle - \langle \Phi_s(\mathbf{r} | \mathbf{r}_0) \rangle \langle \Phi_s^*(\mathbf{r}' | \mathbf{r}_0) \rangle \\ & \approx \sum_{m=1}^{\infty} \sum_{n=1}^{\infty} \langle \Phi_s^{(m,n)}(\mathbf{r} | \mathbf{r}_0) \Phi_s^{(m,n)*}(\mathbf{r}' | \mathbf{r}_0) \rangle \\ & \quad - \langle \Phi_s^{(m,n)}(\mathbf{r} | \mathbf{r}_0) \rangle \langle \Phi_s^{(m,n)*}(\mathbf{r}' | \mathbf{r}_0) \rangle, \end{aligned} \quad (13)$$

where the quadrupole modal sum reduces to a double modal sum.

D. The field scattered from a randomly rough or inhomogeneous seabed

When the scattering is due to a randomly rough seafloor patch, a great simplification occurs in the form of the mutual intensity. Of the 16 parenthetical terms of Eq. (10), only 1 represents a down-going incident wave coupling to an up-going scattered wave. Accordingly, the field scattered into the waveguide from a randomly rough seafloor patch of area ΔA , as defined in Appendix A, must have mutual intensity given by Eq. (9) with

$$\begin{aligned} & \langle \Phi_s^{(m,n)}(\mathbf{r} | \mathbf{r}_0) \Phi_s^{(m',n')*}(\mathbf{r}' | \mathbf{r}_0) \rangle \\ & = \left(\frac{4\pi}{k} \right)^2 [B_m(\mathbf{r}) A_n(\mathbf{r}_0) B_{m'}^*(\mathbf{r}') A_{n'}^*(\mathbf{r}_0) \\ & \quad \times \langle S(\alpha_m, \phi; \alpha_n, \phi_0 + \pi) S^*(\alpha_{m'}, \phi'; \alpha_{n'}, \phi_0 + \pi) \rangle], \end{aligned} \quad (14)$$

and cross spectral density given by Eq. (11) with

$$\begin{aligned} & \langle \Phi_s^{(m,n)}(\mathbf{r} | \mathbf{r}_0) \Phi_s^{(m',n')*}(\mathbf{r}' | \mathbf{r}_0) \rangle - \langle \Phi_s^{(m,n)}(\mathbf{r} | \mathbf{r}_0) \rangle \langle \Phi_s^{(m',n')*}(\mathbf{r}' | \mathbf{r}_0) \rangle \\ & = \left(\frac{4\pi}{k} \right)^2 B_m(\mathbf{r}) A_n(\mathbf{r}_0) B_{m'}^*(\mathbf{r}') A_{n'}^*(\mathbf{r}_0) \{ \langle S(\alpha_m, \phi; \alpha_n, \phi_0 + \pi) S^*(\alpha_{m'}, \phi'; \alpha_{n'}, \phi_0 + \pi) \rangle \\ & \quad - \langle S(\alpha_m, \phi; \alpha_n, \phi_0 + \pi) \rangle \langle S^*(\alpha_{m'}, \phi'; \alpha_{n'}, \phi_0 + \pi) \rangle \}. \end{aligned} \quad (15)$$

The cross spectral density is more useful in describing the stochastic scattering properties of a randomly rough seafloor patch than the mutual intensity because deterministic effects, such as specular reflection, coherent beaming, and forward scattering, are removed with the expected field. In diffuse surface scattering problems, where the surface scattering patch must be much larger than the wavelength, the expected value of the scattered field is typically negligible away from the specular direction due to random interference. The cross spectral density and mutual intensity then become effectively indistinguishable.

With the assumption of diffuse scattering described in the previous section, which is supported by a large amount of experimental evidence,^{18,22} application of Eq. (12a) yields

$$\begin{aligned} & \langle \Phi_s^{(m,n)}(\mathbf{r} | \mathbf{r}_0) \Phi_s^{(m',n')*}(\mathbf{r}' | \mathbf{r}_0) \rangle \\ & \quad - \langle \Phi_s^{(m,n)}(\mathbf{r} | \mathbf{r}_0) \rangle \langle \Phi_s^{(m',n')*}(\mathbf{r}' | \mathbf{r}_0) \rangle \\ & = \delta_{mm'} \delta_{nn'} C_{mn}(\mathbf{r}, \mathbf{r}' | \mathbf{r}_0) B_m(\mathbf{r}) A_n(\mathbf{r}_0) B_{m'}^*(\mathbf{r}') A_{n'}^*(\mathbf{r}_0) \\ & \quad \times \left(\frac{4\pi}{k} \right)^2, \end{aligned} \quad (16)$$

which leads to a great simplification in the scattered field covariance:

$$\begin{aligned} & \langle \Phi_s(\mathbf{r} | \mathbf{r}_0) \Phi_s^*(\mathbf{r}' | \mathbf{r}_0) \rangle - \langle \Phi_s(\mathbf{r} | \mathbf{r}_0) \rangle \langle \Phi_s^*(\mathbf{r}' | \mathbf{r}_0) \rangle \\ & = \left(\frac{4\pi}{k} \right)^2 \sum_{m=1}^{\infty} \sum_{n=1}^{\infty} B_m(\mathbf{r}) B_m^*(\mathbf{r}') |A_n(\mathbf{r}_0)|^2 C_{mn}(\mathbf{r}, \mathbf{r}' | \mathbf{r}_0). \end{aligned} \quad (17)$$

If the seafloor is taken as an aggregate of range-dependent scattering patches and if these are each small enough to have little effect on the mean forward field, Eq. (17) provides a good approximation to the cross spectral density after forward propagating through this mildly range-dependent waveguide and then scattering in a specified direction from the given patch.

It is noteworthy that a formulation in terms of wave number integrals is not convenient in describing the statistical equipartition of energy associated with diffuse scattering since the modes are the entities that describe the system's degrees of freedom rather than the wave number components.

E. General saddle point approximation for the scattered field in time from a distant object

For a source with general time dependence

$$q(t) = \int_{-\infty}^{\infty} Q(f) e^{-i2\pi ft} df, \quad (18)$$

and spectrum

$$Q(f) = \int_{-\infty}^{\infty} q(t) e^{i2\pi ft} dt, \quad (19)$$

the scattered field as a function of time from an object with center at the origin becomes

$$\Psi_s(\mathbf{r}|\mathbf{r}_0|t) = \int_{-\infty}^{\infty} Q(f) \Phi_s(\mathbf{r}|\mathbf{r}_0) e^{-i2\pi ft} df, \quad (20)$$

where Eq. (1) can be rewritten as

$$\Phi_s(\mathbf{r}|\mathbf{r}_0) = \sum_{m=1} \sum_{n=1} \Lambda_{mn}(\mathbf{r}|\mathbf{r}_0, f) e^{i\rho_0 \xi_n + i\rho \xi_m}, \quad (21)$$

so that

$$\Psi_s(\mathbf{r}|\mathbf{r}_0|t) = \sum_{m=1} \sum_{n=1} \int_{-\infty}^{\infty} Q(f) \Lambda_{mn}(\mathbf{r}|\mathbf{r}_0, f) e^{i\rho \psi_{mn}(f)} df, \quad (22)$$

where

$$\Lambda_{mn}(\mathbf{r}|\mathbf{r}_0, f) = \Phi_s^{(m,n)}(\mathbf{r}|\mathbf{r}_0) e^{-i\rho_0 \xi_n - i\rho \xi_m}, \quad (23)$$

and

$$\psi_{mn}(f) = \frac{\rho_0}{\rho} \xi_n + \xi_m - 2\pi f \frac{t}{\rho}. \quad (24)$$

By application of the saddle point method, for large ρ , assuming ρ_0/ρ and t/ρ are fixed,

$$\begin{aligned} \Psi_s(\mathbf{r}|\mathbf{r}_0|t) &\approx \sum_{l=1} \sum_{m=1} \sum_{n=1} \sqrt{\frac{2\pi}{\rho \psi''(f_{lmn})}} \\ &\quad \times Q(f_{lmn}) \Lambda_{nm}(\mathbf{r}|\mathbf{r}_0, f_{lmn}) \\ &\quad \times e^{i\rho \psi_{mn}(f_{lmn}) + (\pm i\pi/4)_{lmn}}, \end{aligned} \quad (25)$$

where the relevant saddle points f_{lmn} are determined by solving the equation

$$\left. \frac{d\psi_{mn}(f)}{df} \right|_{f=f_{lmn}} = 0, \quad (26)$$

and choosing the complex roots that lead to a finite solution of Eq. (24) as ρ and ρ_0 increase, where l is the index for multiple roots given n and m . Such solutions do not exist before the wave packet has arrived or after it has passed the receiver. Equation (24) can also be written more conveniently as

$$\begin{aligned} \Psi_s(\mathbf{r}|\mathbf{r}_0|t) &\approx \sum_{l=1} \sum_{m=1} \sum_{n=1} Q(f_{lmn}) \sqrt{\frac{2\pi}{\rho \psi''(f_{lmn})}} \\ &\quad \times \Phi_s^{(n,m)}(\mathbf{r}|\mathbf{r}_0)|_{f=f_{lmn}} e^{-i2\pi t f_{lmn} + (\pm i\pi/4)_{lmn}}, \end{aligned} \quad (27)$$

where the frequencies f_{lmn} for each n to m mode conversion must be evaluated at each time and source and receiver range. Equation (27) is also obtained if, analogously, ρ_0 is made large and t/ρ_0 held fixed in Eqs. (22)–(24). Typically, both ρ and ρ_0 will be sufficiently large for the saddle point method approximation to hold whenever the modal formulation of Sec. II A, which also requires large ρ and ρ_0 , is valid.

The covariance of the scattered field at time t from a distant stochastic target then becomes

$$\begin{aligned} &\langle \Psi_s(\mathbf{r}|\mathbf{r}_0|t) \Psi_s^*(\mathbf{r}'|\mathbf{r}_0|t) \rangle - \langle \Psi_s(\mathbf{r}|\mathbf{r}_0|t) \rangle \langle \Psi_s^*(\mathbf{r}'|\mathbf{r}_0|t) \rangle \\ &\approx \sum_{l=1} \sum_{m=1} \sum_{n=1} \sum_{l'=1} \sum_{m'=1} \sum_{n'=1} Q(f_{lmn}) Q^*(f_{l'm'n'}) \\ &\quad \times \frac{2\pi}{\sqrt{\rho \rho' \psi''(f_{lmn}) \psi''^*(f_{l'm'n'})}} \\ &\quad \times e^{-i2\pi t(f_{lmn} - f_{l'm'n'}^*) + (\pm i\pi/4)_{lmn} - (\pm i\pi/4)_{l'm'n'}} \\ &\quad \times \{ \langle \Phi_s^{(m,n)}(\mathbf{r}|\mathbf{r}_0)|_{f=f_{lmn}} \Phi_s^{(m',n')*}(\mathbf{r}'|\mathbf{r}_0)|_{f=f_{l'm'n'}} \rangle \\ &\quad - \langle \Phi_s^{(m,n)}(\mathbf{r}|\mathbf{r}_0)|_{f=f_{lmn}} \rangle \langle \Phi_s^{(m',n')*}(\mathbf{r}'|\mathbf{r}_0)|_{f=f_{l'm'n'}} \rangle \} \end{aligned} \quad (28)$$

by substitution of Eq. (1a) as appropriate for the given scattering scenario.

It can now be seen that the basic equation of Ref. 3, Eq. (9), which appears without stated restrictions, is not generally valid, except under certain narrow-band conditions. Also, the present analysis indicates that the group velocity cannot generally be treated as a frequency-independent quantity as it is in the development of Ref. 3, where a number of narrow-band assumptions have apparently been made implicitly, as may be seen by also consulting Refs. 7 and 23, for example.

F. An absolute reference frame

To compute reverberation from wide and heterogeneous areas of seafloor or a number of distributed scatterers, it is convenient to recast Eq. (1) in terms of an absolute, rather than target-centered, spatial coordinate system. Let this system be defined by coordinates $\mathbf{R}=(X, Y, Z)$ whose axes are

parallel to those of the x, y, z target-centered system, where the positive Z axis is again downward pointing, but whose origin lies at the ocean surface, for example, where $z = -D$ in the target-oriented frame. In this more general frame, the source position is defined by $\mathbf{R}_0 = (X_0, Y_0, Z_0)$, the receiver positions by $\mathbf{R}_r = (X_r, Y_r, Z_r)$ and $\mathbf{R}'_r = (X'_r, Y'_r, Z'_r)$, and the center of a given scattering patch by $\mathbf{R} = (X, Y, Z)$, where, for example, $X = R \sin \vartheta \cos \varphi$, $Y = R \sin \vartheta \sin \varphi$, $Z = R \cos \vartheta$, and $R^2 = X^2 + Y^2 + Z^2$. The origin of all these coordinate systems are colocated and the axes are parallel. Spatial coordinates are translated from the target-oriented to the absolute frame by substituting $\mathbf{r} = \mathbf{R}_r - \mathbf{R}$, $\mathbf{r}' = \mathbf{R}'_r - \mathbf{R}$, and $\mathbf{r}_0 = \mathbf{R}_0 - \mathbf{R}$ in Eqs. (1) and (2). This leads, for example, to

$$A_m(\mathbf{R}_r - \mathbf{R}) = \frac{i u_m (Z_r - Z) N_m^-}{d(Z) (8 \pi \xi_m \sqrt{(X_r - X)^2 + (Y_r - Y)^2})^{1/2}} \times e^{i(\xi_m \sqrt{(X_r - X)^2 + (Y_r - Y)^2} + \gamma_m Z - \pi/4)}, \quad (29a)$$

$$B_m(\mathbf{R}_r - \mathbf{R}) = \frac{i u_m (Z_r - Z) N_m^+}{d(Z) (8 \pi \xi_m \sqrt{(X_r - X)^2 + (Y_r - Y)^2})^{1/2}} \times e^{i(\xi_m \sqrt{(X_r - X)^2 + (Y_r - Y)^2} - \gamma_m Z - \pi/4)} \quad (29b)$$

by making the substitutions

$$\begin{aligned} x_0 &= (X_0 - X), & y_0 &= (Y_0 - Y), \\ x &= (X_r - X), & y &= (Y_r - Y), \\ \rho_0 &= \sqrt{(X_0 - X)^2 + (Y_0 - Y)^2}, \\ \rho &= \sqrt{(X_r - X)^2 + (Y_r - Y)^2}, \\ z_0 &= Z_0 - Z, & z &= Z_r - Z, \end{aligned} \quad (30a)$$

in Eqs. (1) and (2), where

$$\begin{aligned} \cos \phi_0 &= x_0 / \rho_0, & \sin \phi_0 &= y_0 / \rho_0, \\ \cos \phi &= x / \rho, & \sin \phi &= y / \rho. \end{aligned} \quad (30b)$$

It must be stressed that the plane wave amplitudes and vertical wave numbers are evaluated in the layer of the scattering patch. The covariance of the scattering function for a given patch in the absolute, rather than object-oriented frame then becomes

$$C_{mn}(\mathbf{R}_r - \mathbf{R}, \mathbf{R}'_r - \mathbf{R} | \mathbf{R}_0 - \mathbf{R}) = C_{mn}(\mathbf{r}, \mathbf{r}' | \mathbf{r}_0). \quad (31)$$

III. SHALLOW WATER REVERBERATION

A. Reverberation in time

Reverberation, as measured with an active sonar system, is taken to be any and all echoes returning from the environment rather than the intended target. The characteristics of reverberation then depend not only on the environment but also the geometry of the source and receiver as well as the signal waveform. In field measurements, reverberation is measured as a function of time. It can often be decomposed into two components. The most prevalent is a diffuse component. This has instantaneous intensity that typically undergoes random fluctuations that obey the central limit theorem about an expected value that decays uniformly with time. For

reverberation to be diffuse, the scattering region that contributes to the intensity measured at a given instant must be large compared to the mean wavelength. This region, referred to as the system resolution footprint, will be considerably smaller for data beamformed with a high-resolution array than for data received by an omni-directional receiver. The second component, known as clutter, is here defined as any discrete temporal event, caused by an anomalous scatterer, that stands significantly above the diffuse reverberation background. Here ‘‘significantly above’’ means much more than one standard deviation in sound pressure level. For certain systems that employ high-resolution temporal processing and operate in weakly dispersive waveguides, there may be no diffuse component to the reverberation. In this case coherent temporal oscillations may be found in reverberant intensity measurements²⁴ that are due to modal interference as noted by Ellis.³ Lepage has recently investigated similar coherent effects under a narrow-band approximation for an omni-directional receiver.⁷

When the single-scatter approximation is valid, the total reverberant field measured at any time t for a time-harmonic source is simply the sum of the scattered fields from all environmental scatterers

$$\begin{aligned} \Phi_T(\mathbf{R}_r, \mathbf{R}_0) e^{-i2\pi f t} \\ = e^{-i2\pi f t} \int \int \int_V \Phi_s(\mathbf{R}_r - \mathbf{R} | \mathbf{R}_0 - \mathbf{R}) dX dY dZ. \end{aligned} \quad (32)$$

For a source with general time dependence $q(t)$, the total reverberant field becomes

$$\Psi_T(\mathbf{R}_r, \mathbf{R}_0 | t) = \int_{-\infty}^{\infty} Q(f) \Phi_T(\mathbf{R}_r, \mathbf{R}_0) e^{-i2\pi f t} df, \quad (33)$$

or equivalently

$$\Psi_T(\mathbf{R}_r, \mathbf{R}_0 | t) = \int \int \int_V \Psi_s(\mathbf{R}_r - \mathbf{R} | \mathbf{R}_0 - \mathbf{R} | t) dX dY dZ, \quad (34)$$

where $\Psi_s(\mathbf{R}_r - \mathbf{R} | \mathbf{R}_0 - \mathbf{R} | t)$ can be obtained directly from Eq. (25) for distant scatterers. The simplicity of this equation is deceptive. While it can be evaluated in a relatively straightforward manner for deterministic targets, its interpretation and implementation become far more difficult for stochastic targets. The covariance

$$\begin{aligned} \langle \Psi_T(\mathbf{R}_r, \mathbf{R}_0 | t) \Psi_T^*(\mathbf{R}'_r, \mathbf{R}_0 | t') \rangle \\ - \langle \Psi_T(\mathbf{R}_r, \mathbf{R}_0 | t) \rangle \langle \Psi_T^*(\mathbf{R}'_r, \mathbf{R}_0 | t') \rangle, \end{aligned}$$

for example, provides a second moment characterization of the reverberant field that is sufficient for most remote sensing applications, where a statistical correlation between scatterers over the volume V is implicitly required to evaluate the covariance. This quantity is most useful for investigating the performance of systems that employ pulse compression in an attempt to attain high temporal resolution. If all scatterers are independent, the covariance of the total reverberant field in

time can be obtained directly by summing the covariances of the individual scatterers using Eq. (28).

A difficulty arises, however, in any *analytic* representation for $\langle \Psi_T(\mathbf{R}_r, \mathbf{R}_0|t) \Psi_T^*(\mathbf{R}'_r, \mathbf{R}_0|t') \rangle$ when expectation values are brought within the modal sums and spatial and Fourier integrals. Even for a single random scattering patch, one finds that the second moment of the scatter-function, $\langle S(\theta, \phi; \theta_i, \phi_i) |_{f} S^*(\theta', \phi'; \theta'_i, \phi'_i) |_{f'} \rangle$, is required for *joint* correlation across both wave number and frequency. We are only aware of analytic derivations existing for this second moment when $\theta = \theta'$, $\phi = \phi'$, $\theta_i = \theta'_i$, $\phi_i = \phi'_i$, and $f = f'$, as noted in the definition of the expected bistatic scattering cross section of a random target or rough surface patch in Appendix A. This difficulty is circumvented when $\langle \Psi_T(\mathbf{R}_r, \mathbf{R}_0|t) \Psi_T^*(\mathbf{R}'_r, \mathbf{R}_0|t') \rangle$ is estimated by Monte Carlo simulation since $\Psi_T(\mathbf{R}_r, \mathbf{R}_0|t) \Psi_T^*(\mathbf{R}'_r, \mathbf{R}_0|t')$ is averaged across independent realizations of the rough surface. Broadband scattering statistics can then be obtained by either the saddle point method of Sec. II E or the Fourier synthesis of Eq. (20) since only the deterministic scatter function need be known to compute the scattered field for a given realization of the rough surface. In this way, by Monte Carlo simulations, $\langle \Psi_T(\mathbf{R}_r, \mathbf{R}_0|t) \Psi_T^*(\mathbf{R}'_r, \mathbf{R}_0|t') \rangle$ can be readily obtained using the theory developed in Sec. II to investigate the performance of systems that employ high-resolution temporal processing such as pulse compression.

B. Charting diffuse reverberation when system integration time spans dominant signal energy

A simpler analytic approach than the saddle point approximation or Fourier synthesis can be employed to investigate system performance when the integration time of the measurement system T is sufficiently long to include the dominant signal energy returned from the target or scattering patch. In this case, Parseval's theorem can be applied to the Fourier integral of Eq. (20), converted to absolute coordinates, to obtain the time-averaged mutual intensity expected at \mathbf{R}_r from a target or scattering patch at \mathbf{R} due to a source at \mathbf{R}_0 ,

$$\begin{aligned} I(\mathbf{R}, \mathbf{R}_r, \mathbf{R}_0, t) &= \frac{1}{T} \int_{t-T/2}^{t+T/2} \langle |\Psi_s(\mathbf{R}_r - \mathbf{R} | \mathbf{R}_0 - \mathbf{R} | t_0)|^2 \rangle dt_0 \\ &\approx \frac{1}{T} \int_{-\infty}^{\infty} \langle |\Psi_s(\mathbf{R}_r - \mathbf{R} | \mathbf{R}_0 - \mathbf{R} | t_0)|^2 \rangle dt_0 \\ &= \frac{1}{T} \int_{-\infty}^{\infty} |Q(f)|^2 \langle |\Phi_s(\mathbf{R}_r - \mathbf{R} | \mathbf{R}_0 - \mathbf{R})|^2 \rangle df, \end{aligned} \quad (35)$$

where $t - T/2$ is less than or equal to the arrival time of the scattered signal.

This type of incoherent integration is typically used in the reception of narrow-band source waveforms, and is also often used in the analysis of broadband returns from explosive sources such as SUS²² where the exact time function of the source is unknown. While it is equally valid for waveforms of arbitrary bandwidth, it does not take advantage of

the full pulse compression possible for broadband waveforms. However, it is often unclear in practice whether or not pulse compression can be meaningfully exploited with signals received after dispersive waveguide propagation. For the type of incoherent time average specified in Eq. (35), the problems mentioned in Sec. III A are alleviated since only $\langle S(\theta, \phi; \theta_i, \phi_i) |_{f} S^*(\theta', \phi'; \theta'_i, \phi'_i) |_{f'} \rangle$ need be evaluated for a given random scatterer, so that Eqs. (9) and (10) can be directly applied, since frequency cross terms vanish as a result of Parseval's theorem. A center frequency approximation to Eq. (35) can often be made for narrow-band signals as discussed in Appendix B.

If the time spread of the signal due to dispersion in the waveguide $\Delta \tau_s$ is small compared to the time duration T_s of the source signal, the expected horizontal range resolution $\Delta \rho$ of the system will take roughly the same form as in free space $\Delta \rho = \bar{c} T_s / 2$, for narrow-band signals, where \bar{c} is the mean horizontal propagation speed of the signal between source and receiver in the waveguide. In this case, the integration time T of the system can be set to its minimum value of T_s . Both $\Delta \tau_s$ and \bar{c} can be quantitatively defined in terms of the received field as in Ref. 25. They depend on the acoustic properties of the waveguide, the signal time dependence, and source-receiver geometry. For the narrow-band examples of Sec. IV, simulations show that $\bar{c} \approx 1500$ m/s, $t\bar{c} \approx \rho + \rho_0$, and $\Delta \tau_s / T_s$ is small, where ρ and ρ_0 are defined in Eq. (30a).

A typical bistatic sonar system will resolve a patch of seafloor $A(\mathbf{R}, \mathbf{R}_r, \mathbf{R}_0)$, the dimensions of which depend on the receiving array aperture, frequency, and the bistatic geometry of the source, receiver, and seafloor patch as discussed in Appendix C of Ref. 26 and Refs. 27 and 28. For a monostatic measurement $A = \rho \Delta \rho \Delta \varphi$, where $\Delta \varphi = \lambda / L_A$ is the Rayleigh resolution of the horizontal aperture of length L_A .

For convenience, assume that the *horizontal* origin in an absolute reference frame is chosen to be at the center of the receiving array $\mathbf{Z}_r = (0, 0, Z_r)$. Let the beamformed output of a receiving array located along the Y_r -axis, obtained by spatial Fourier transform of the time-harmonic scattered field across the array aperture, be denoted by

$$\begin{aligned} \Phi_B(\phi_s, Z_r, \mathbf{R}, \mathbf{R}_0) &= \int_{-\infty}^{\infty} T(Y_r) Q(f) \Phi_s(\mathbf{R}_r - \mathbf{R} | \mathbf{R}_0 - \mathbf{R}) \\ &\quad \times e^{ik \sin \varphi_s Y_r} dY_r, \end{aligned} \quad (36)$$

where φ_s is the azimuth the array is steered towards, φ is the azimuth of the scattering patch, and $T(Y_r)$ is the array taper function. Suppose a uniform rectangular taper function is used with $T(Y_r) = 1/L_A$ for $-L_A/2 \leq Y_r \leq L_A/2$ and zero elsewhere, and the seafloor scattering patch is in the far field of the array, such that $|\mathbf{R}| > L_A^2 / \lambda$, and the scattering patch behaves as a point target to the array so that the angle it subtends at the array is less than λ / L_A . Under these assumptions, the spectral density or field variance received from this patch can be well approximated by

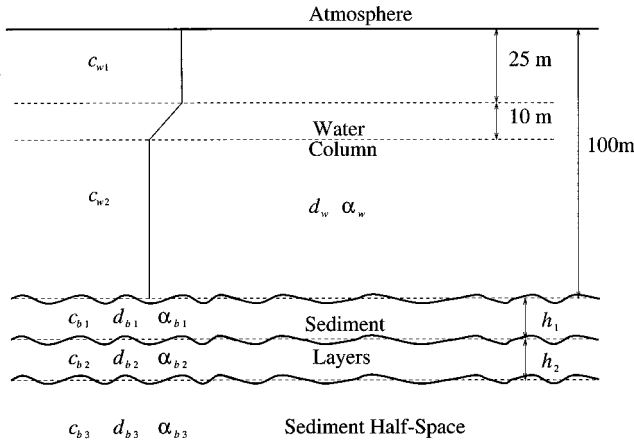


FIG. 1. The geometry of the waveguide which has a water column comprised of upper layer sound speed c_{w1} for $0 < Z < 25$, lower layer sound speed c_{w2} for $35 < Z < 100$, and transition layer sound speed $c_{w1} - (c_{w1} - c_{w2})(Z - 25)/10$ for $25 \leq Z \leq 35$. The water column density is $d_w = 1000 \text{ kg/m}^3$ and the attenuation is $\alpha_w = 6.0 \times 10^{-5} \text{ dB/\lambda}$. The bottom can have up to two sediment layers. The upper and middle sediment layers have respective thicknesses, sound speeds, densities, and attenuations of h_1 , c_{b1} , d_{b1} , α_{b1} and h_2 , c_{b2} , d_{b2} , α_{b2} , overlying a sediment half-space of sound speed c_{b3} , density d_{b3} , and attenuation α_{b3} . The monopole source is collocated with receiving array center, with array axis normal to the range-depth plane of the sketch. Source and receiver may be placed anywhere in the water column. The submerged target may be placed in the upper or lower layers of the water column where sound speed is constant as indicated in Fig. 2. Seafloor and buried riverbank features may also be included at the water-sediment and sediment-layer to sediment half-space interfaces as indicated in Fig. 6. Squiggly lines indicate statistically rough interfaces.

$$\begin{aligned}
 & \langle |\Phi_B(\varphi, Z_r, \mathbf{R}, \mathbf{R}_0)|^2 \rangle - \langle \Phi_B(\varphi, Z_r, \mathbf{R}, \mathbf{R}_0) \rangle^2 \\
 &= \left(\frac{4\pi}{k} \right)^2 |Q(f)|^2 \sum_{m=1}^{\infty} \sum_{n=1}^{\infty} |B_m(\mathbf{Z}_r - \mathbf{R})|^2 \\
 & \quad \times |A_n(\mathbf{R}_0 - \mathbf{R})|^2 C_{mn}(\mathbf{Z}_r - \mathbf{R}, \mathbf{Z}_r - \mathbf{R} | \mathbf{R}_0 - \mathbf{R}) \\
 & \quad \times \left| \frac{\sin\{(L_A/2) \sin \varphi [k - \text{Re}\{\xi_m\}]\}}{(L_A/2) \sin \varphi [k - \text{Re}\{\xi_m\}]} \right|^2 \quad (37)
 \end{aligned}$$

upon substitution of Eq. (17) into Eq. (36) with $\phi_s = \phi$ so the array is steered toward the patch. With the assumption that the resolution footprint A is much larger than ΔA , the area of a given patch, and all patches are statistically independent, the total variance of the received field from seafloor within the system resolution footprint can be written as the sum of the variances of each patch via

$$\begin{aligned}
 V_B(X, Y) &= \iint_{A(\mathbf{R}, Z_r, \mathbf{R}_0)} \langle |\Phi_B(\varphi, Z_r, \mathbf{R}', \mathbf{R}_0)|^2 \rangle \\
 & \quad - \langle \Phi_B(\varphi, Z_r, \mathbf{R}', \mathbf{R}_0) \rangle^2 \frac{1}{n_z' \Delta A} dX' dY', \quad (38)
 \end{aligned}$$

where $\hat{n} = (n_x, n_y, n_z)$ is the surface normal at \mathbf{R} . Since the differential area $dX' dY'$ must be normalized by the horizontal projected area of each potentially inclined patch at \mathbf{R}' to allow horizontal integration, Eq. (38) does not allow vertical patches.

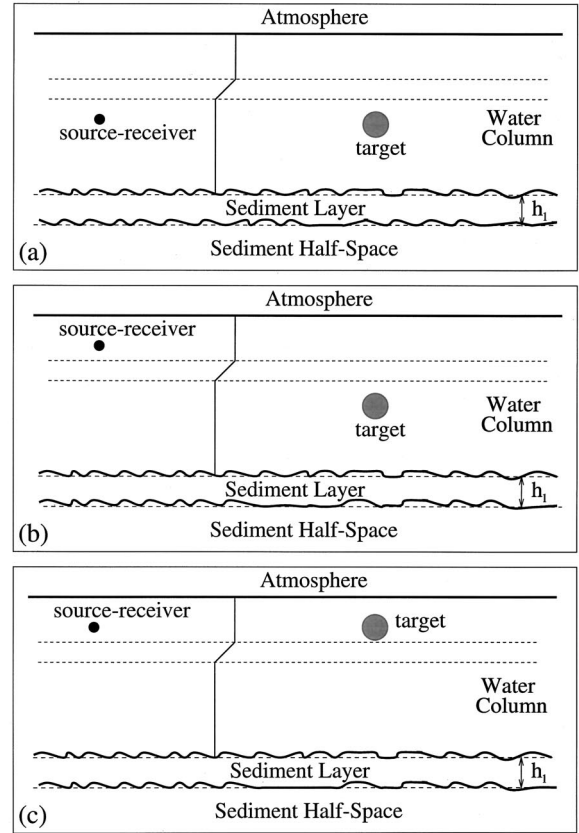


FIG. 2. Three scenarios for the active detection of a submerged pressure release sphere of radius $a = 10 \text{ m}$. The water column is modeled as either having constant sound speed or as downward refracting. The bottom is composed of either a pure sediment half-space or a single sediment layer over a sediment half-space. (a) Monopole source and horizontal receiving array center are collocated at 50-m depth with target at 50-m depth. (b) Source and receiving array center are collocated at 10-m depth with target at 50-m depth. (c) Source and receiving array center are collocated at 10-m depth with target at 15-m depth.

When Parseval's theorem is invoked again under the assumption that the integration time of the measurement system includes the dominant energy returned from the resolved patch of seafloor, after time-domain beamforming and finite time averaging by the receiver over period T , the field variance from seafloor within the system resolution footprint of area $A(\mathbf{R}, \mathbf{R}_r, \mathbf{R}_0)$ centered at (X, Y) becomes

$$\bar{V}_B(X, Y) = \frac{1}{T} \int_{-\infty}^{\infty} V_B(X, Y) df. \quad (39)$$

Equations (37)–(39) imply a reduction in reverberation level for off-broadside beams due solely to modal dispersion. Only at broadside does the phase speed of the incident waves match that expected under the nondispersive assumptions of plane wave beamforming. Only broadside beamforming is considered in the simulations of the present article to eliminate this effect from the analysis. The effects of modal dispersion on beamformed reverberation are investigated in Ref. 25.

Under the present assumptions, reverberation measured in time can be charted in space for any bistatic geometry using a look-up table comprised of the mean time delay from source to scattering patch $\bar{\tau}(\mathbf{r}_t, \mathbf{r}_0)$ and scattering patch to

receiver $\bar{r}(\mathbf{r}, \mathbf{r}_r)$.²⁵ Similarly, reverberation modeled with the spatial formulation of Eqs. (38) and (39) can be made a function of time by reversing the procedure.

C. Lambert–Mackenzie scattering and reverberation

A number of simplifications are possible when the scattering surface has *Lambertian*²⁹ behavior. The covariance of the scattering function for a Lambertian scattering patch of area ΔA with albedo ε takes the form of Eq. (12a) with

$$C_{lm}(\mathbf{R}_r - \mathbf{R}, \mathbf{R}'_r - \mathbf{R} | \mathbf{R}_0 - \mathbf{R}) = k^2 \frac{\varepsilon}{\pi} |\hat{i}_{sl} \cdot \hat{n}| |\hat{i}_{im} \cdot \hat{n}| \Delta A, \quad (40)$$

where \hat{i}_{im} and \hat{i}_{sl} are the directions in which the down-going component of the m th incident and up-going component of the l th scattered modes propagate and \hat{n} is the seafloor normal, pointing away from the water column, in a scattering-patch-centered coordinate system where the positive- z axis points downward. The differential scattering cross section of the surface patch is then given by the product of $4\pi/k^2$ and the right-hand side of Eq. (40).

Under Lambertian scattering, the cross spectral density of the scattered field given in Eq. (17) then becomes expressible in terms of single summations

$$\begin{aligned} & \langle \Phi_s(\mathbf{r}) \Phi_s^*(\mathbf{r}') \rangle - \langle \Phi_s(\mathbf{r}) \rangle \langle \Phi_s^*(\mathbf{r}') \rangle \\ &= 16\pi\varepsilon\Delta A \left(\sum_{l=1}^{\infty} B_l(\mathbf{r}) B_l^*(\mathbf{r}') |\hat{i}_{sl} \cdot \hat{n}| \right) \\ & \quad \times \left(\sum_{m=1}^{\infty} |A_m(\mathbf{r}_0)|^2 |\hat{i}_{im} \cdot \hat{n}| \right). \end{aligned} \quad (41)$$

The surface projection factors can be written in terms of the incident and scattered wave number components, the measurement geometry, and the orientation of the surface patch via

$$|\hat{i}_{sl} \cdot \hat{n}| = \left| \frac{\xi_l}{k} [n_x \cos \varphi + n_y \sin \varphi] + \frac{\gamma_l}{k} n_z \right|, \quad (42a)$$

$$|\hat{i}_{im} \cdot \hat{n}| = \left| \frac{\xi_m}{k} [n_x \cos(\varphi_0 + \pi) + n_y \sin(\varphi_0 + \pi)] - \frac{\gamma_m}{k} n_z \right|. \quad (42b)$$

The scattered field covariance from a given seafloor patch in a target-oriented frame is

$$\begin{aligned} & \langle \Phi_s(\mathbf{r} | \mathbf{r}_0) \Phi_s^*(\mathbf{r}' | \mathbf{r}_0) \rangle - \langle \Phi_s(\mathbf{r} | \mathbf{r}_0) \rangle \langle \Phi_s^*(\mathbf{r}' | \mathbf{r}_0) \rangle \\ &= 16\pi\varepsilon\Delta A \left(\sum_{l=1}^{\infty} B_l(\mathbf{r}) B_l^*(\mathbf{r}') \left| \frac{\xi_l}{k} [n_x \cos \varphi + n_y \sin \varphi] \right. \right. \\ & \quad \left. \left. + \frac{\gamma_l}{k} n_z \right| \right) \left(\sum_{m=1}^{\infty} |A_m(\mathbf{r}_0)|^2 \left| \frac{\xi_m}{k} [n_x \cos(\varphi_0 + \pi) \right. \right. \\ & \quad \left. \left. + n_y \sin(\varphi_0 + \pi)] - \frac{\gamma_m}{k} n_z \right| \right), \end{aligned} \quad (43)$$

where $n_x = n_y = 0$ for a bottom with zero mean inclination. In an absolute frame it becomes

$$\begin{aligned} & \langle \Phi_s(\mathbf{R}_r - \mathbf{R} | \mathbf{R}_0 - \mathbf{R}) \Phi_s^*(\mathbf{R}'_r - \mathbf{R} | \mathbf{R}_0 - \mathbf{R}) \rangle - \langle \Phi_s(\mathbf{R}_r - \mathbf{R} | \mathbf{R}_0 - \mathbf{R}) \rangle \langle \Phi_s^*(\mathbf{R}'_r - \mathbf{R} | \mathbf{R}_0 - \mathbf{R}) \rangle \\ &= 16\pi\varepsilon\Delta A \left(\sum_{l=1}^{\infty} B_l(\mathbf{R}_r - \mathbf{R}) B_l^*(\mathbf{R}'_r - \mathbf{R}) \left| \frac{\xi_l}{k} \frac{n_x(X_r - X) + n_y(Y_r - Y)}{\sqrt{(X_r - X)^2 + (Y_r - Y)^2}} + \frac{\gamma_l}{k} n_z \right| \right) \\ & \quad \times \left(\sum_{m=1}^{\infty} |A_m(\mathbf{R}_0 - \mathbf{R})|^2 \left| \frac{\xi_m}{k} \frac{n_x(X_0 - X) + n_y(Y_0 - Y)}{\sqrt{(X_0 - X)^2 + (Y_0 - Y)^2}} + \frac{\gamma_m}{k} n_z \right| \right), \end{aligned} \quad (44)$$

where the components of the surface normal \hat{n} are now a function of the X, Y, Z position of the surface patch center. Under far-field assumption, the field variance received from seafloor within the system resolution footprint centered at (X, Y) and averaged over time period T can be well approximated by

$$\begin{aligned} \bar{V}_B(X, Y) &= \frac{16\pi\varepsilon}{T} \int_{-\infty}^{\infty} |Q(f)|^2 \int \int_{A(\mathbf{R}, \mathbf{Z}_r, \mathbf{R}_0)} \left(\sum_{l=1}^{\infty} |B_l(\mathbf{Z}_r - \mathbf{R}')|^2 \left| \frac{\xi_l}{k} \frac{n_x(X_r - X') + n_y(Y_r - Y')}{\sqrt{(X_r - X')^2 + (Y_r - Y')^2}} + \frac{\gamma_l}{k} \right| \right. \\ & \quad \left. \times \left| \frac{\sin((L_A/2) \sin \varphi [k - \text{Re}\{\xi_l\}])}{(L_A/2) \sin \varphi [k - \text{Re}\{\xi_l\}]} \right|^2 \right) \left(\sum_{m=1}^{\infty} |A_m(\mathbf{R}_0 - \mathbf{R}')|^2 \left| \frac{\xi_m}{k} \frac{n_x(X_0 - X') + n_y(Y_0 - Y')}{\sqrt{(X_0 - X')^2 + (Y_0 - Y')^2}} + \frac{\gamma_m}{k} \right| \right) dX' dY' df, \end{aligned} \quad (45)$$

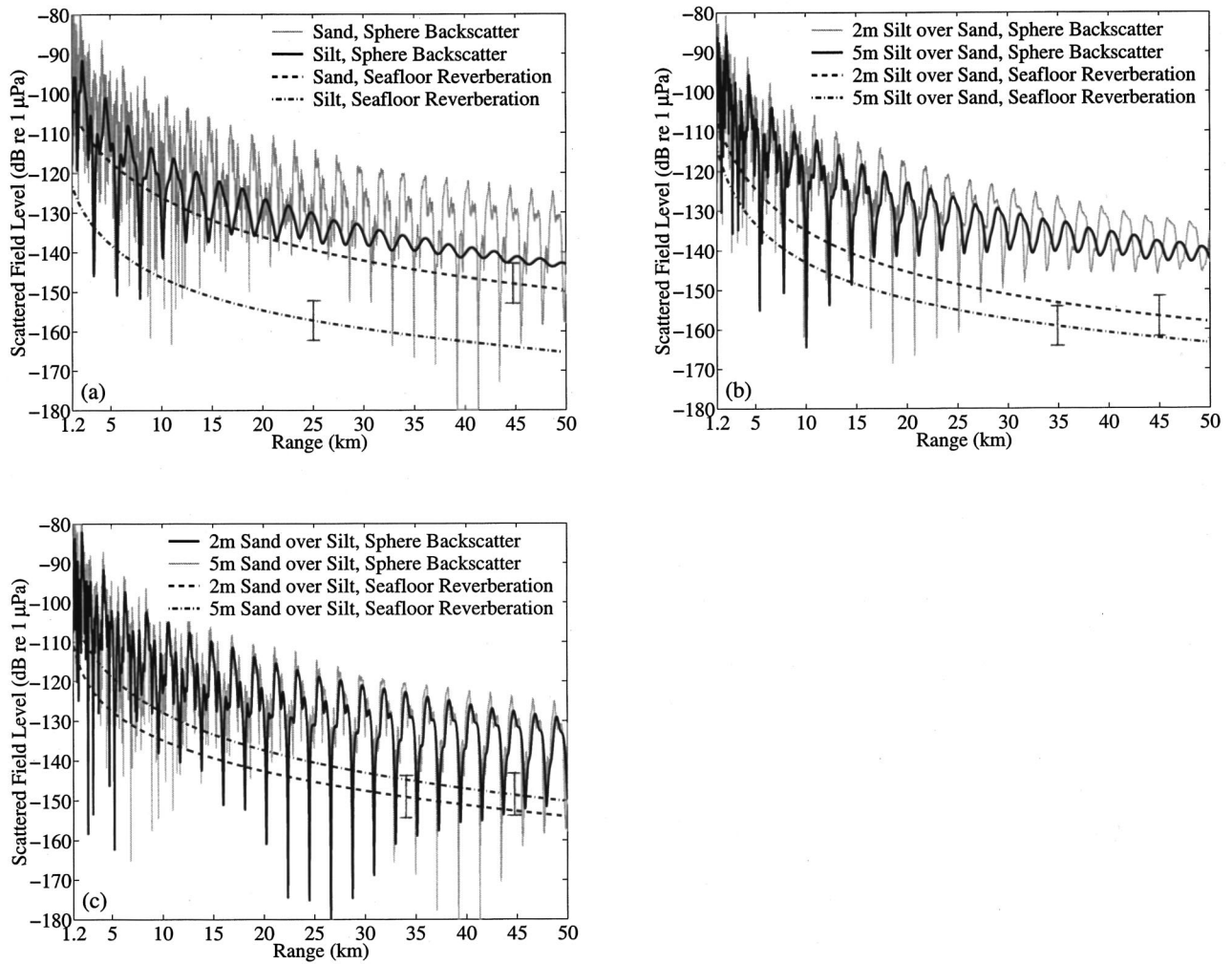


FIG. 3. The scattered field from a submerged pressure-release sphere of radius $a = 10$ m, at $f = 300$ Hz and center at 50-m depth, and Lambert–Mackenzie reverberation from the seafloor within the broadside resolution footprint of the monostatic system as a function of range for a water column with constant sound speed of 1500 m/s, i.e., $c_{w1} = c_{w2} = 1500$ m/s. Monopole source and receiving array center are collocated at 50-m depth. Range increases along the x -axis and depth along the z -axis, with the array axis along the y -axis. Source strength is 0 dB re 1 μ Pa @ 1 m. Reverb modeled with $T = 1/2$ s duration cw source signal at 300 Hz and receiving array resolution $\lambda/L = 3.7$ degrees. (a) Pekeris waveguide examples for bottom half-spaces composed of either sand or silt, i.e., $h_1 = h_2 = 0$. (b) Bottom has a silt layer of either $h_1 = 2$ m or $h_1 = 5$ m overlying a sand half-space, and $h_2 = 0$. (c) Bottom has a sand layer of either $h_1 = 2$ m or $h_1 = 5$ m overlying a silt half-space, and $h_2 = 0$. Error bars show the 5.6 dB standard deviation in reverb level.

when T is sufficiently large for the dominant energy of the scattered field to be received. This result for the Lambertian seafloor offers significant advantages in implementation through the separation of the incident and scattered modal summations. For narrow-band waveforms, terms within the modal summations of Eq. (45) often vary so slowly that they can be approximated as a constant function of frequency over the dominant portion of the spectral window $Q(f)$. This greatly simplifies computations as shown in Appendix B.

D. Perturbation theory for diffuse rough surface scattering and reverberation

Perturbation theory can also be used to calculate the field scattered by a rough surface. The advantage of perturbation theory, when it is applicable, is that it is derived from first principles and so requires knowledge of only the geoacoustic properties of the media, such as sound speed and density, as well as a second moment characterization of the statistical properties of the scattering surface.

Let the x and y components of the gradient of the surface $z_s(x, y)$ be denoted by

$$p = \frac{\partial z_s}{\partial x}, \quad (46a)$$

$$q = \frac{\partial z_s}{\partial y}. \quad (46b)$$

The surface normal can be expressed as

$$\mathbf{n} = \frac{(-p, -q, 1)}{\sqrt{1 + p^2 + q^2}}, \quad (47a)$$

along with two orthonormal surface tangents

$$\mathbf{t}_1 = \frac{(1, 0, p)}{\sqrt{1 + p^2}}, \quad (47b)$$

and

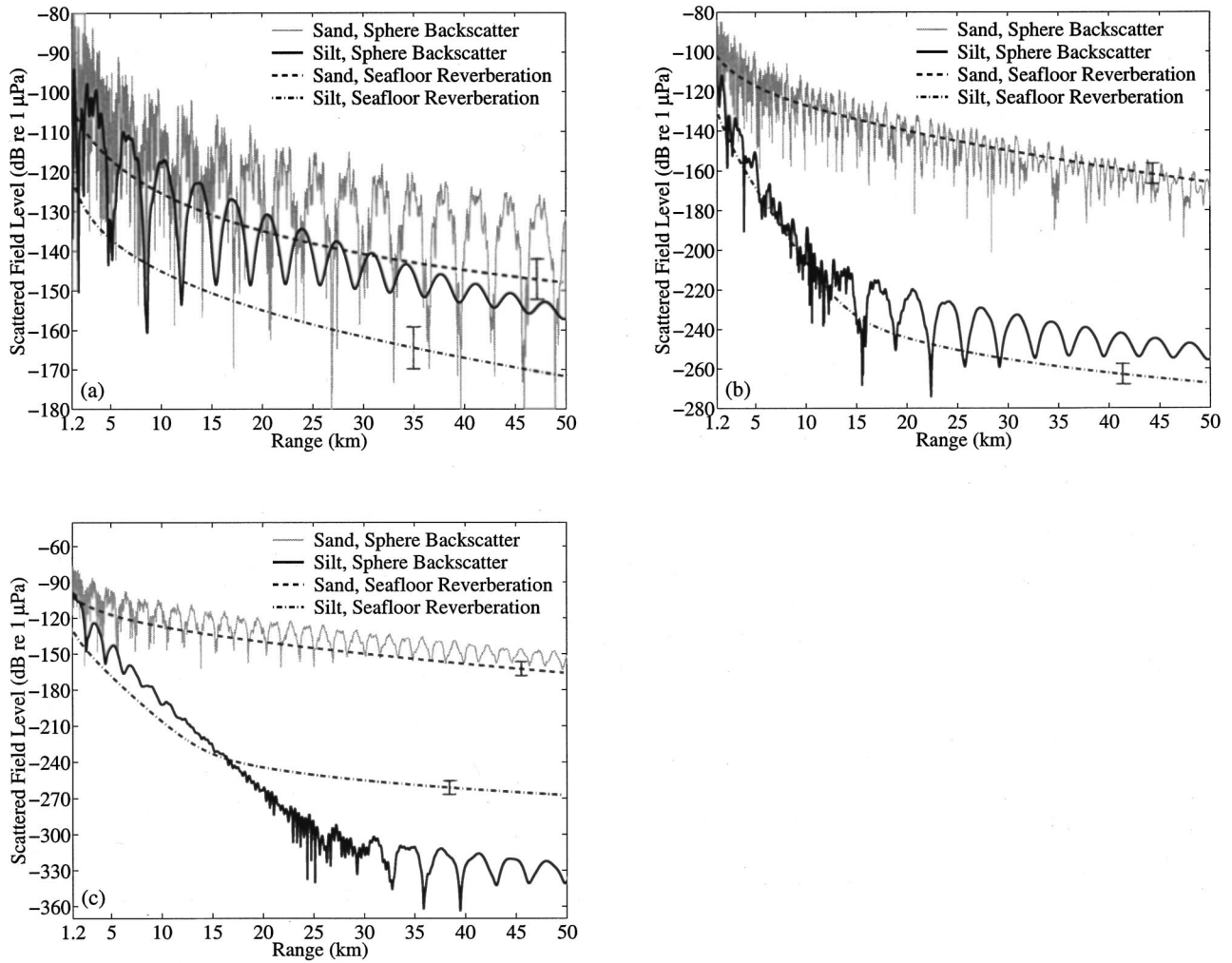


FIG. 4. Same as Fig. 3 except water column is layered with $c_{w1} = 1520$ m/s and $c_{w2} = 1500$ m/s and monostatic source–receiver as well as target sphere are at variable depth. Only the cases of pure sand or pure silt bottom half-spaces are shown. (a) Source–receiver and sphere center are at 50-m depth. (b) Source–receiver are at 10-m depth while sphere center is at 50-m depth. (c) Source–receiver are at 10-m depth while sphere center is at 15-m depth.

$$\mathbf{t}_2 = \frac{(-pq, 1+p^2, q)}{\sqrt{(1+p^2)(1+p^2+q^2)}}, \quad (47c)$$

where \mathbf{t}_1 is obtained by taking an infinitesimal step along the surface on the x axis, and \mathbf{t}_2 is the crossproduct of \mathbf{n} and \mathbf{t}_1 .

The projections of the incident and scattered wave number vectors on the surface then become

$$\mathbf{K}_i = (\mathbf{k}_i \cdot \mathbf{t}_1)\mathbf{t}_1 + (\mathbf{k}_i \cdot \mathbf{t}_2)\mathbf{t}_2, \quad (48a)$$

$$\mathbf{K} = (\mathbf{k} \cdot \mathbf{t}_1)\mathbf{t}_1 + (\mathbf{k} \cdot \mathbf{t}_2)\mathbf{t}_2, \quad (48b)$$

where, for incident mode n and scattered mode m ,

$$\mathbf{k}_i = (\xi_n \cos(\phi_0 + \pi), \xi_n \sin(\phi_0 + \pi), \gamma_n), \quad (49a)$$

$$\mathbf{k} = (\xi_m \cos \phi, \xi_m \sin \phi, \gamma_m), \quad (49b)$$

so that

$$\mathbf{K}_i \cdot \mathbf{K} = (\mathbf{k}_i \cdot \mathbf{t}_1)(\mathbf{k} \cdot \mathbf{t}_1) + (\mathbf{k}_i \cdot \mathbf{t}_2)(\mathbf{k} \cdot \mathbf{t}_2), \quad (50)$$

and, for example,

$$|\mathbf{K}_i|^2 = (\mathbf{k}_i \cdot \mathbf{t}_1)^2 + (\mathbf{k}_i \cdot \mathbf{t}_2)^2, \quad (51a)$$

$$|\mathbf{K}|^2 = (\mathbf{k} \cdot \mathbf{t}_1)^2 + (\mathbf{k} \cdot \mathbf{t}_2)^2. \quad (51b)$$

A plane wave incident from medium 1 half-space that is reflected from strata below has total reflection coefficient³⁰

$$\Gamma(\mathbf{K}_i) = \frac{\Gamma_{12}(\mathbf{K}_i) + \Gamma'(\mathbf{K}_i)e^{i2\gamma^{(2)}h_1}}{1 + \Gamma_{12}(\mathbf{K}_i)\Gamma'(\mathbf{K}_i)e^{i2\gamma^{(2)}h_1}}, \quad (52a)$$

where

$$\Gamma_{12}(\mathbf{K}_i) = \frac{\rho_2 / \sqrt{k_2^2 - K_i^2} - \rho_1 / \sqrt{k_1^2 - K_i^2}}{\rho_2 / \sqrt{k_2^2 - K_i^2} + \rho_1 / \sqrt{k_1^2 - K_i^2}} \quad (52b)$$

is the reflection coefficient from the medium 1 to medium 2 interface, $\Gamma'(\mathbf{K}_i)$ is the total reflection coefficient from all strata below medium 2 for a plane wave incident from medium 2, h_1 is the thickness of the layer containing medium 2, and $\gamma^{(2)}$ is the vertical wave number component of medium 2.

The differential scattering cross section of a surface patch of area ΔA , from first-order perturbation theory, can be expressed as³⁰

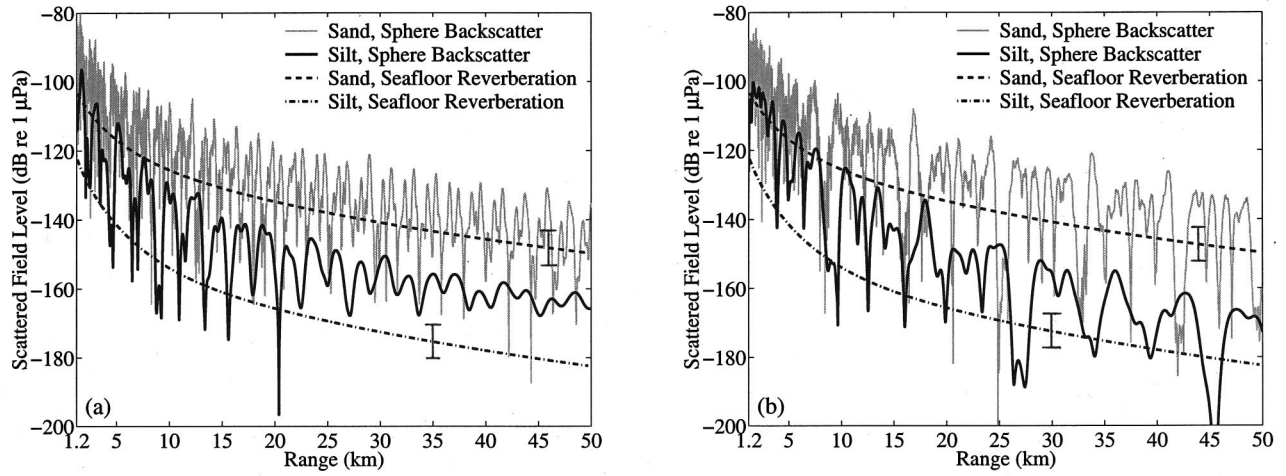


FIG. 5. Pekeris waveguide with varying source–receiver and target depth. (a) Same as Fig. 3(a) except source–receiver is at 10-m depth and target is at 50-m depth. (b) Same as Fig. 3(a) except source–receiver is at 10-m depth and target is at 15-m depth.

$$\sigma_{\text{pert}}(\alpha, \beta; \alpha_i, \beta_i) = 4\pi\Delta A \left(\frac{k_1^4}{4} \right) \left| [\Gamma(\mathbf{K}) + 1][\Gamma(\mathbf{K}_i) + 1] \right|^2 \left| 1 - \frac{\kappa^2}{d_{bt}} + \left(\frac{1}{d_{bt}} - 1 \right) \left(\frac{\mathbf{K} \cdot \mathbf{K}_i}{k_1^2} - \frac{P_g^2(\mathbf{k}, \mathbf{k}_i, \mathbf{n})}{d_{bt}} \right) \right|^2 W(\mathbf{K} - \mathbf{K}_i), \quad (53)$$

where

$$P_g^2(\mathbf{K}, \mathbf{K}_i) = d_{bt}^2 \frac{|\mathbf{k}_i \cdot \mathbf{n}|}{k_i} \frac{|\mathbf{k} \cdot \mathbf{n}|}{k} \left(\frac{1 - \Gamma(\mathbf{K}_i)}{1 + \Gamma(\mathbf{K}_i)} \right) \left(\frac{1 - \Gamma(\mathbf{K})}{1 + \Gamma(\mathbf{K})} \right), \quad (54)$$

and

$$d_{bt} = d_b / d_t, \quad (55)$$

$$\kappa = \kappa_t / \kappa_b, \quad (56)$$

where d_t and d_b are the respective densities above and below the scattering interface and κ_t and κ_b the respective wave number magnitudes above and below the scattering interface.

Following Moe and Jackson,³⁰ the roughness of the given surface patch is assumed to follow the isotropic power law

$$W(\mathbf{K}) = w_2 |\mathbf{K}|^{-\gamma}. \quad (57)$$

With the assumption that the scattering patch is much greater than the wavelength so that the incident and scattered modes are decorrelated by the scattering process, the covariance of the scatter function is given by Eq. (12a) with

$$C_{mn}(\mathbf{r}, \mathbf{r}' | \mathbf{r}_0) = \frac{k^2}{4\pi} \sigma_{\text{pert}}(\alpha_m, \phi; \alpha_n, \phi_0 + \pi). \quad (58)$$

Upon substituting Eq. (58) into Eqs. (17), or (38) after beam-

forming, it is found that the covariance of the field scattered from a rough surface patch that obeys first-order perturbation theory involves a double summation over the waveguide modes. Evaluating this is significantly more computationally intensive than the product of single modal summations found in the Lambert–Mackenzie formulation.

E. Coherent reverberation from deterministic and stochastic geological features

There are two general kinds of seafloor scatterers that do not decorrelate the incident or scattered modes. A seafloor scatterer of the first kind can be modeled as a deterministic feature, with known or computable far-field scatter function, that can have arbitrary size compared to the wavelength so long as it falls within the resolution footprint of the active sonar system. The feature must be distinct from the otherwise range-independent boundaries of the stratified medium in order to induce scattering.

A compelling canonical example of a seafloor scatterer of the first kind is a smooth flat inclined segment of the seafloor, such as a seafloor or subseafloor river channel, iceberg scour, or submerged hillside, that can be modeled as a flat plate with scattering characteristics determined by its size, inclination, and the local geo-acoustic properties of the interface. The 3-D scatter function for a rectangular surface patch with total reflection coefficient $\Gamma(\mathbf{K}_i)$, for example, can be readily determined by applying Green's theorem, Eq. (A1), for a plane wave, with wave number magnitude k_1 , incident in the direction (α_i, β_i) and a far-field receiver in the direction (α, β) with respect to the patch centroid. If the patch is assumed to be at inclination χ from horizontal, where the angle χ comprises a counter-clockwise rotation about the y axis, the scatter function takes the form

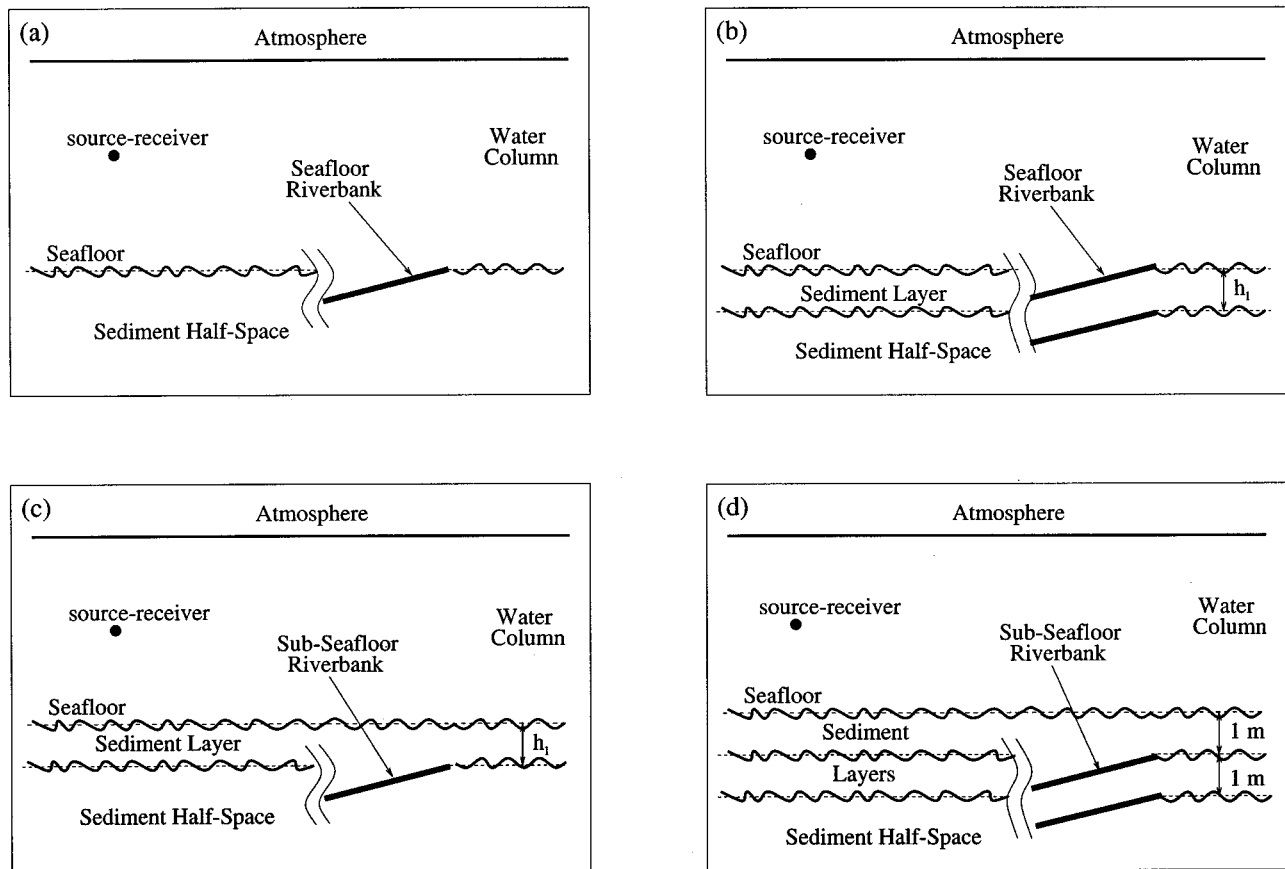


FIG. 6. Scenarios for the active detection of seafloor and subseafloor riverbank features. The water column is modeled as having constant sound speed, i.e., $c_{w1} = c_{w2} = 1500$ m/s, and monopole source and horizontal receiving array center are collocated at 50-m depth in all cases. (a) Bottom is sediment half-space with seafloor feature, i.e., $h_1 = h_2 = 0$. (b) Bottom is composed of a single sediment layer with double-interface seafloor feature, i.e., $h_2 = 0$. (c) Bottom is composed of a single sediment layer with subseafloor feature, i.e., $h_2 = 0$. (d) Bottom is composed of two sediment layers with double-interface subseafloor feature.

$$S(\alpha, \beta; \alpha_i, \beta_i) = i \frac{k_1^2}{4\pi} L_x L_y \left[(1 - \Gamma(\mathbf{K}_i)) \{ \cos \alpha_i \cos \chi + \sin \alpha_i \sin \chi \cos \beta_i \} + (1 + \Gamma(\mathbf{K}_i)) \{ \cos \alpha \cos \chi + \sin \alpha \sin \chi \cos \beta \} \right] \times \text{sinc} \left[\frac{k_1 L_x}{2} \{ (\sin \alpha_i \cos \beta_i \cos \chi - \cos \alpha_i \sin \chi) - (\sin \alpha \cos \beta \cos \chi - \cos \alpha \sin \chi) \} \right] \text{sinc} \left[\frac{k_1 L_y}{2} \{ \sin \alpha_i \sin \beta_i - \sin \alpha \sin \beta \} \right], \quad (59)$$

where $\text{sinc}(x)$ is defined as $\sin x/x$. The reflection coefficient can be determined from Eq. (52) with the understanding that, in the present geometry, the squared magnitude of the transverse component of the incident wave number vector on the inclined surface patch is

$$K_i^2 = k_1^2 - k_1^2 (\cos \alpha_i \cos \chi + \sin \alpha_i \sin \chi \cos \beta_i)^2. \quad (60)$$

Irregularities in the surface can make its scatter function deviate from that given in Eq. (59). For realistic seafloor and subseafloor riverbanks, however, it is reasonable to assume that, for a low-frequency active system²⁸ at long range in a shallow water waveguide where propagation is near horizontal, the product of the amplitude of such irregularities and the normal component of the wave number vector with respect to the surface will be small enough that the irregularities will have a negligible effect on the field from the riverbank.

A seafloor scatterer of the second kind is a randomly rough rather than deterministic feature but is appropriately modeled with completely coherent modes when the ratio of wavelength to system range resolution, $\lambda/\Delta\rho$, is near or greater than the equivalent vertical propagation angle of the highest order trapped mode, which in many shallow water scenarios is roughly the bottom critical angle. This situation occurs for active sonar systems with high range-resolution and can lead to the formation of range-dependent rings in charted reverberant intensity caused by modal interference.²⁴ (Lepage⁷ has recently described scenarios in which such rings can form even in narrow-band reverberation at short ranges.) The level of returns can be estimated by appropriately modeling the seafloor scatter function. If the system resolution footprint extends over many wavelengths in any direction and the correlation length of surface roughness is

much smaller than the system resolution footprint, then the scattering function for the seafloor over this area can be treated as a fluctuating target. If the resolution footprint is on the order of the wavelength or the correlation length of surface roughness, a quasi-deterministic description of the scattering process can be used.

IV. ILLUSTRATIVE EXAMPLES

In all the illustrative examples of this section, a water column of 100-m depth is used to simulate a typical continental shelf environment. The sound speed structure of the water column varies from iso-velocity to downward refracting layers with constant density of 1 g/cm^3 and attenuation of $6.0 \times 10^{-5} \text{ dB}/\lambda$. The seabed is comprised of sand or silt half-spaces, with up to two sediment layers, comprised of sand or silt, over a sand or silt half-space. The density, sound speed and attenuation are taken to be 1.9 g/cm^3 , 1700 m/s , and $0.8 \text{ dB}/\lambda$ for sand, 1.4 g/cm^3 , 1520 m/s , and $0.3 \text{ dB}/\lambda$ for silt, and 1.2 g/cm^3 , 1510 m/s , and $0.3 \text{ dB}/\lambda$ for light-silt. Scattering and reverberation calculations are made for a submerged target, roughness at the water–seabed interface, roughness at the interface between the upper seabed layer and lower half-space, as well as for anomalous features of the seafloor or subseafloor that return geological clutter. The latter are taken to be seafloor river banks at the water–seabed interface or subseafloor riverbanks at the interface between the upper sediment layer and lower half-space. The geometry of the waveguide is sketched in Fig. 1.

A horizontal line array with $N=32$ equally spaced elements of length $L_A=(N-1)\lambda/2$ at $f=300 \text{ Hz}$ is used as a receiver and a cw pulse of $T=\frac{1}{2}$ -s duration centered at f

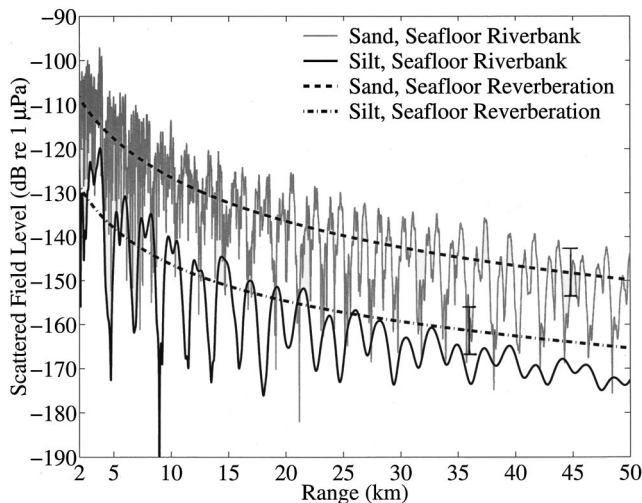


FIG. 7. The field at $f=300 \text{ Hz}$ scattered from a coherently scattering rectangular patch of area $100 \times 100 \text{ m}^2$ representing a seafloor riverbank for scenario shown in Fig. 6(a), constant sound speed water column over pure silt or sand half-spaces. Range increases along the x axis and depth along the z axis. The square riverbank surface has two edges parallel to the y axis, and is inclined 10° from the x axis. Constant sound speed in the water column is assumed for all examples with $c_{w1}=c_{w2}=1500 \text{ m/s}$. Lambert–Mackenzie reverberation within the range-dependent resolution footprint of the monostatic system is also shown separately for the water–sediment interface (seafloor). Source strength is $0 \text{ dB re } 1 \mu\text{Pa}$ @ 1 m . Diffuse reverb modeled with $T=1/2$ s duration cw source signal at 300 Hz and receiving array resolution $\lambda/L=3.7$ degrees.

$=300 \text{ Hz}$ is used as a source waveform for all simulations of diffuse reverberation. Targets beyond L_A^2/λ are in the far field of the array, which begins at roughly 1.2 km . The beamformed field from an object that falls within the broadside beam of the array, in the absence of other sources or scatterers, equals the field received from that object by a single hydrophone at the array center when Eq. (36) is used with uniform taper $T(Y_r)=1/L_A$. If the same object is placed at the same range but within an off-broadside beam, a reduction in the beamformed output may occur due to modal dispersion, as is discussed in detail in Ref. 25. For simplicity, only objects and reverberation within the broadside beam are considered in the present article. Only monostatic scenarios are considered, where the source is located at the center of the receiving array. This leads to a range-dependent resolution footprint $A=\rho\Delta\rho\Delta\varphi$, where $d\rho=cT/2=375 \text{ m}$ and $d\varphi=\lambda/L_A\approx 3.7$ degrees for the given array, frequency, and cw pulse length.

A center frequency approximation, at $f=300 \text{ Hz}$, is made for all scattering calculations. For reverberation calculations this approximation differs from the full spectral integration by less than 0.1 dB for the examples shown. As may be expected in coherent scattering from targets where modal interference is significant, some range-dependent nulls and valleys in the sound pressure level of the received field found in the single frequency calculation may be partially filled when the full bandwidth is used for the narrow-band waveforms considered. Since this filling is window dependent, as shown in Appendix B, only center frequency calculations are presented in the main text. It is also shown in Appendix B that in some valleys of some single frequency calculations the target returns may fall below the expected reverberation level but will be above this level when the full bandwidth of a given narrow-band window function is employed.

Only the empirical Lambert–Mackenzie model is used in comparisons between seafloor reverberation and submerged-object returns since insufficient data on the requisite environmental parameters at low frequency are available to make a similar comparison with perturbation theory meaningful. Perturbation theory calculations are only used self-consistently to make inferences about the relative level of returns from different kinds of seafloor scatterers.

A. Submerged target echo versus diffuse reverberation level for varying source–receiver depth, target depth, water column, and bottom stratification

The geometry for active detection of a sphere submerged in an ocean waveguide is sketched in Fig. 2 for the illustrative examples of this section. The geometry is monostatic with co-located omni-directional point source and receiving array centers at 50-m depth. The sphere center is also at $D=50\text{-m}$ depth at array broadside with variable horizontal range. The field back scattered from a pressure release sphere of radius $a=10 \text{ m}$ at $f=300 \text{ Hz}$ is shown as a function of range in Figs. 3(a)–(c) in decibels, i.e., $20 \log|\Phi_s|$, for various bottom types under a water column with constant sound speed $c_w=1500 \text{ m/s}$, where $c_{w1}=c_{w2}=1500 \text{ m/s}$. The scattered field is computed by Eq. (1), with scatter function

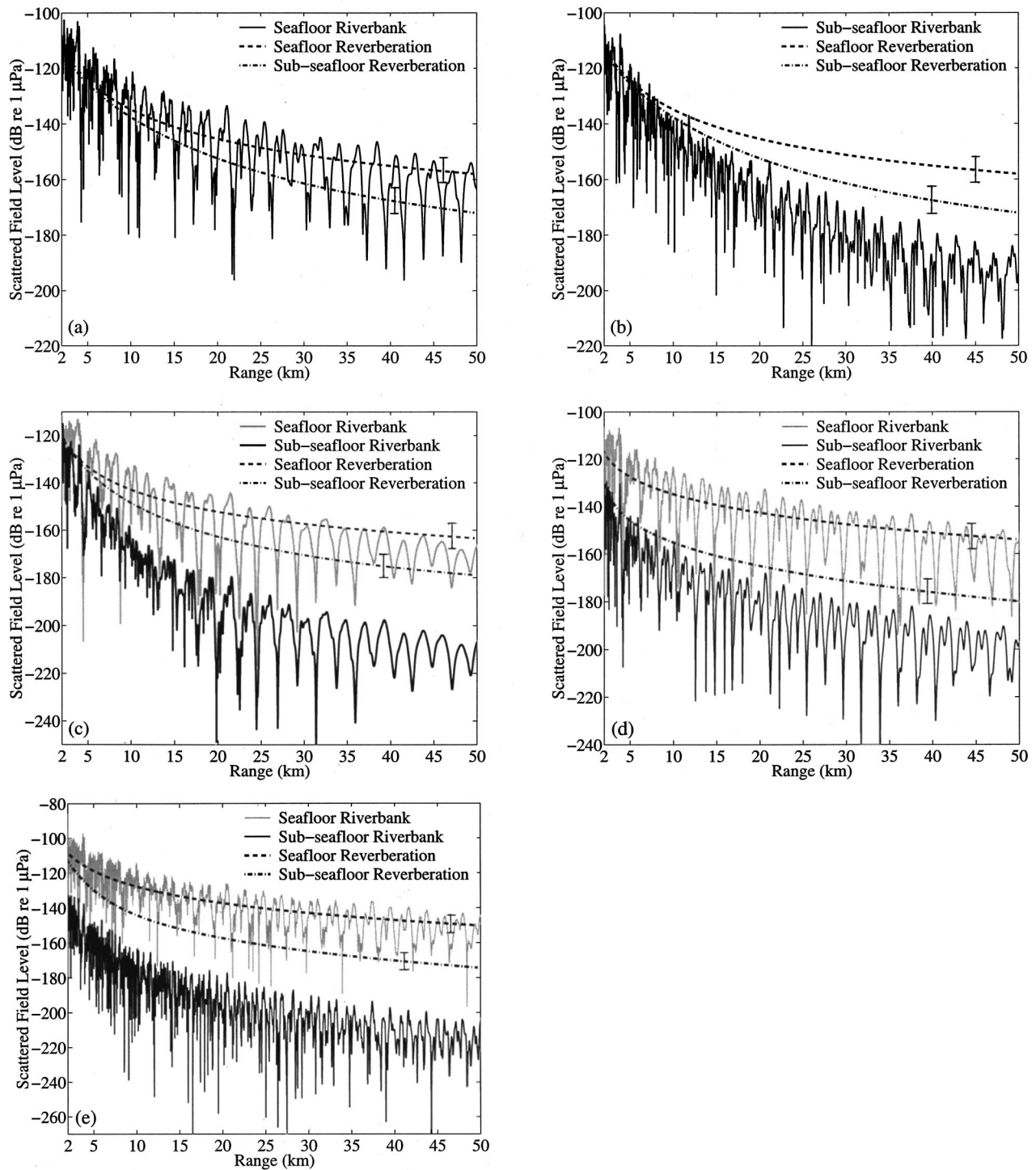


FIG. 8. Same as Fig. 7 except single layer bottom scenarios of Figs. 6(b) and (c) for coherent seafloor and subseafloor riverbank scattering are investigated. Lambert–Mackenzie reverb within the sonar resolution footprint is also shown for the sediment-layer to sediment half-space interface (subseafloor). (a) Seafloor riverbank with the upper sediment layer composed of silt with $h_1=2$ m and the lower sediment half-space composed of sand. Coherent riverbank scattering is from the double interface of water to silt to sand. (b) Subseafloor riverbank with the upper sediment layer composed of silt with $h_1=2$ m and the lower sediment half-space composed of sand. Coherent riverbank scattering is from the single silt to sand interface. (c) Seafloor and subseafloor riverbanks as in (a) and (b) but with the upper sediment layer now at $h_1=5$ m thickness. (d) Same as (c) but with the upper sediment layer composed of sand with $h_1=2$ m and the lower sediment half-space composed of silt. (e) Same as (d) except $h_1=5$ m.

given by Eqs. (8) and (9) of Ref. 11 with $f(n)$ replaced by $(-1)^n f(n)$ to convert from Ingenito's definition to the standard one described in Sec. II A.³¹

The variance of the field scattered from the seafloor

within the range-dependent resolution footprint of the sonar system under the Lambert–Mackenzie assumption of Eq. (45) is also shown in Fig. 3 in decibels, i.e., $10 \log \bar{V}_B$. Modal interference is absent due to the modal decoupling

assumed in diffuse scattering from large seafloor patches. Ambiguous returns from both sides of the line array are included.

The scattered field from both the target sphere and seafloor is highly dependent on the geo-acoustic parameters of the bottom, as is evident in Fig. 3(a) where significant differences arise when the bottom type is changed from sand to silt. The differences arise primarily because the number of trapped modes is significantly larger for the sand half-space due to the higher critical angle of 28.1° for water to sand as compared with the 9.3° for water to silt. This leads to a correspondingly higher mean level, of roughly 20 dB, for both target and seafloor backscatter and a shorter modal interference length scale in the scattered field from the sphere.

In the Pekeris waveguide examples of Fig. 3(a), the target stands tens of decibels above the expected reverberation within the broadside beam regardless of whether the bottom is composed of sand or silt. This signal excess is well above the reverberation level standard deviation of 5.6 dB assuming the seafloor scattering obeys circular complex Gaussian statistics, in accord with the central limit theorem.²¹ If a single omni-directional hydrophone placed at the center of the receiving array replaces the full array, the reverberation levels are augmented by roughly $10 \log(2\pi/d\phi) \approx 20$ dB in Fig. 3. The target sphere then no longer consistently stands above the expected reverberation even at short ranges, for example, within a few kilometers. A directional array is then necessary to spatially filter the target from omni-directional reverberation so that detection can be practically achieved in the given scenarios.

The effect of bottom properties on both submerged target scattering and reverberation is again evident when layered bottoms are considered. For the silt-over-sand scenarios of Fig. 3(b), the characteristics of the field scattered from the target are a combination of those found for the silt and sand half-spaces. As the silt layer increases from roughly one-half to a full wavelength, the rate of modal interference decreases, as does the overall level of the scattered field from both the target and bottom. When the layer thickness reaches a full wavelength, the level of reverberation approaches that obtained for a pure silt bottom as range increases. The low critical angle between the water-silt interface enables greater bottom penetration than is possible with a water-sand interface. The high attenuation of the silt layer then leads to bottom loss that increases with the thickness of the layer.

For the sand-over-silt scenarios of Fig. 3(c), the field scattered from the target greatly resembles that obtained for the pure sand bottom of Fig. 3(a). The match becomes better as the sand layer increases in thickness from one-half to a full wavelength, in which case the reverberation increases from a few decibels below to roughly the level found for a pure sand bottom. In the latter case, the silt half-space is effectively insulated from the water column by evanescent decay of the trapped modes in the sand layer.

The absolute and relative levels of target and reverberation echo returns are highly dependent upon the water column sound speed structure as well as source, receiver, and target depth. To illustrate this, consider the typical shallow water downward refracting profile shown in Fig. 1, with

$c_{w1} = 1520$ m/s, $c_{w2} = 1500$ m/s, and a linear transition region in between, that is similar to what is found in continental shelf waters in late spring and summer months. Monostatic measurements of the field scattered from a 10-m-radius pressure-release sphere are again made with the same array and cw tone used in the previous examples. The target is at array broadside and both target returns and reverb within the broadside beam are plotted as a function of range, where the reverb is computed again for a $T = \frac{1}{2}$ s cw at 300 Hz center frequency. Three combinations of monostatic source-receiver and target depths are considered, as illustrated in Fig. 2.

First consider the case in Fig. 4(a), where the source, receiving array, and sphere center are at 50-m depth just as in the Pekeris waveguide examples. For the sand bottom, the levels are similar to those found in the corresponding example of Fig. 3(a), with the target standing out by tens of decibels. For the silt bottom, the target still stands tens of decibels above the reverberation but the absolute levels of the scattered fields decay more rapidly with range in the present scenario since the downward-refracting profile causes more acoustic energy to penetrate into the bottom.

Loss of energy to the bottom is augmented when the source and receiver array are placed in the mixed layer, at 10-m depth, while the target remains with center at 50-m depth, as shown in Fig. 4(b). The absolute levels of both the field scattered from the target sphere and the seafloor are reduced by tens of decibels beyond a few kilometers' range for the silt bottom. For the sand bottom, the reverberation level is not significantly changed by moving the source and receiver into the mixed layer. Returns from the target sphere, however, no longer stand prominently enough above the expected reverberation to insure detection, given a 5.6-dB standard deviation in reverberation level.

The situation for detection again changes when the target sphere is placed in the mixed layer, with sphere center at 15-m depth, along with the source and receiver at 10-m depth as shown in Fig. 4(c). This is especially so for the silt bottom, where the scattered field from the target sphere becomes so greatly reduced, when compared to the previous examples of this section, that its returns only stand above the expected reverberation level within roughly 16-km range. It is interesting that for the sand bottom, the placement of the target and source-receiver in the mixed layer leads to more favorable conditions for detection, which should be possible beyond 50-km range, than if only the source-receiver were placed in the mixed layer and the target was in the middle of the water column as in Fig. 4(b). This is because the higher-order modes stimulated by the shallow source, receiver, and target can be supported by the high-critical-angle sand bottom.

The exercise of changing the depths of the source-receiver and target is repeated in Fig. 5 for a constant sound speed water column. For the sand bottom, the level of the field scattered from the sphere is not affected significantly by moving the source-receiver and target depths. For the silt bottom, however, a significant decrease in the sphere's echo-return level is found for shallow source-receiver and target placements. Apparently, these shallow placements stimulate

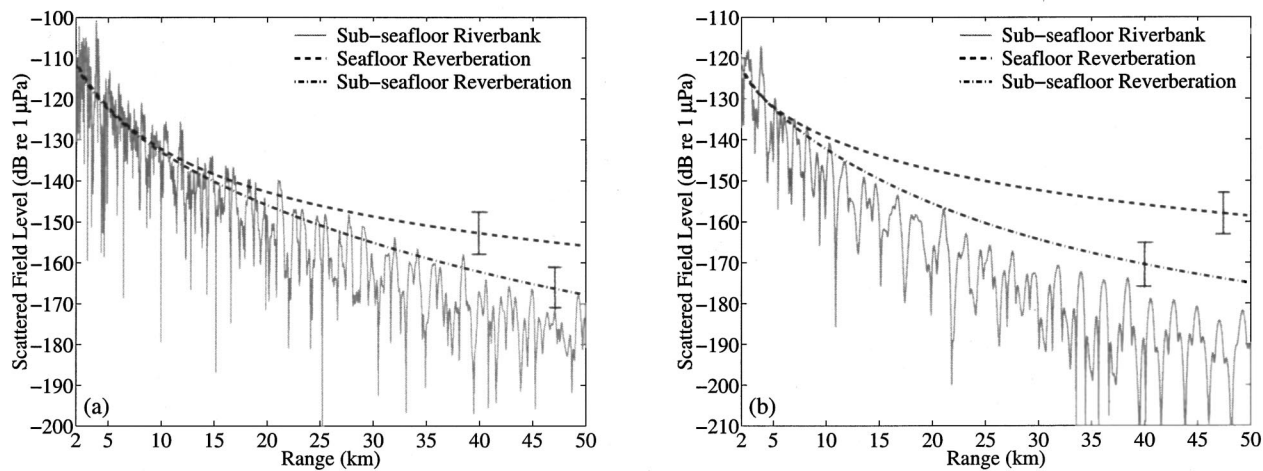


FIG. 9. Same as Fig. 8 except two-layer bottom scenario of Fig. 6(d) is investigated for coherent scattering from subseafloor riverbank. (a) Sediment is comprised of light silt layer of $h_1 = 1$ -m thickness over a silt layer of $h_2 = 1$ -m thickness over a sand half-space. Coherent riverbank scattering is from the double interface of light silt to silt to sand. (b) Sediment is comprised of light silt layer of $h_1 = 1$ -m thickness over a sand layer of $h_2 = 1$ -m thickness over a silt half-space. Coherent riverbank scattering is from the double interface of light silt to sand to silt.

higher-order modes that are not supported by the silt bottom. These results should be compared to those found in Fig. 3(a) for source–receiver and target depths in the middle of the waveguide at 50 m.

B. Geological clutter versus diffuse seafloor reverberation

Geomorphic features of the seafloor can return echoes that stand well above the diffuse reverberation background described in the previous section. Since these echoes appear as discrete events in time or range, they may be used to remotely image seafloor or subseafloor geomorphology in geophysical applications. They may, however, also be confused with returns from a submerged target in an active detection scenario.

Both coherent and incoherent scattering from the canonical seafloor and subseafloor features, shown in Fig. 6, are investigated. Both kinds of features are modeled as a flat 100×100 -m² surfaces at an inclination of 10 degrees. The dimensions and inclination are based on actual geophysical data characterizing seafloor and subseafloor riverbanks.³² Seafloor and subseafloor river channels are commonly found in continental shelf waters after a sea level rise. The latter requires an additional influx of sedimentation. In all cases to be considered here, the waveguide is modeled as an isovelocity water column overlying one or two sediment layers that cover a sediment half space.

For the coherent calculation, the riverbank is treated as a smooth but finite square surface with reflection coefficient appropriate to the given boundary conditions, including multiple reflection from various layers. The coherent scattered field from the riverbank in the layered waveguide follows when the scatter function for the smooth riverbank, given in Eq. (59), is inserted into Eq. (1). Coherent scattering from the riverbank is then completely determined by the boundary conditions at the riverbank and the riverbank geometry. For the incoherent calculation, the riverbank is modeled first as a

diffusely scattering Lambertian surface with the empirically derived Mackenzie albedo and riverbank tilt angle incorporated as indicated in Eq. (41). The diffuse calculations are also made using perturbation theory by substituting Eq. (58) into Eq. (17). In both cases, the assumption is that the seafloor feature falls within the resolution footprint of the sonar system.

Illustrative examples are given in Figs. 7–9, 13, 19, and 20. The geometry is again monostatic with colocated omnidirectional point source and receiving array centers at 50-m depth. The receiving array lies parallel to the y axis. The square riverbank surface has two edges parallel to the y axis, is centered at $y = 0$, and inclined 10 degrees about the x axis. All plots give the scattered field from the riverbank as a function of range from the monostatic sonar. For comparison, incoherent reverberation from the water–sediment interface within the resolution footprint of the sonar, based on the Lambert–Mackenzie model for an un-inclined surface, is also plotted as a function of range in Figs. 7–9 and 13 and based on perturbation theory in Figs. 19 and 20. This is referred to as diffuse seafloor reverberation. The range and cross-range resolution of the sonar system resolution footprint are the same as those stated in the introduction to Sec. IV. Similarly, incoherent reverberation from the sediment layer to sediment half-space interface, based upon the Lambert–Mackenzie model for an uninclined surface, is also plotted as a function of range in Figs. 7–9 and 13, and based on perturbation theory in Figs. 19 and 20. This is referred to as diffuse subseafloor reverberation. The far field of the coherent riverbank begins at roughly 2 km while the far field of the receiving array begins at roughly 1.2 km.

For the Pekeris waveguide scenario of Fig. 6(a), returns from the seafloor riverbank features stand well above diffuse seafloor reverberation from the silt bottom within ranges of roughly 20 km and from the sand bottom beyond ranges of 50 km when the riverbank is treated as a coherent scatterer, as shown in Fig. 7. The ordinate is in decibels, i.e., $20 \log |\Phi_s|$

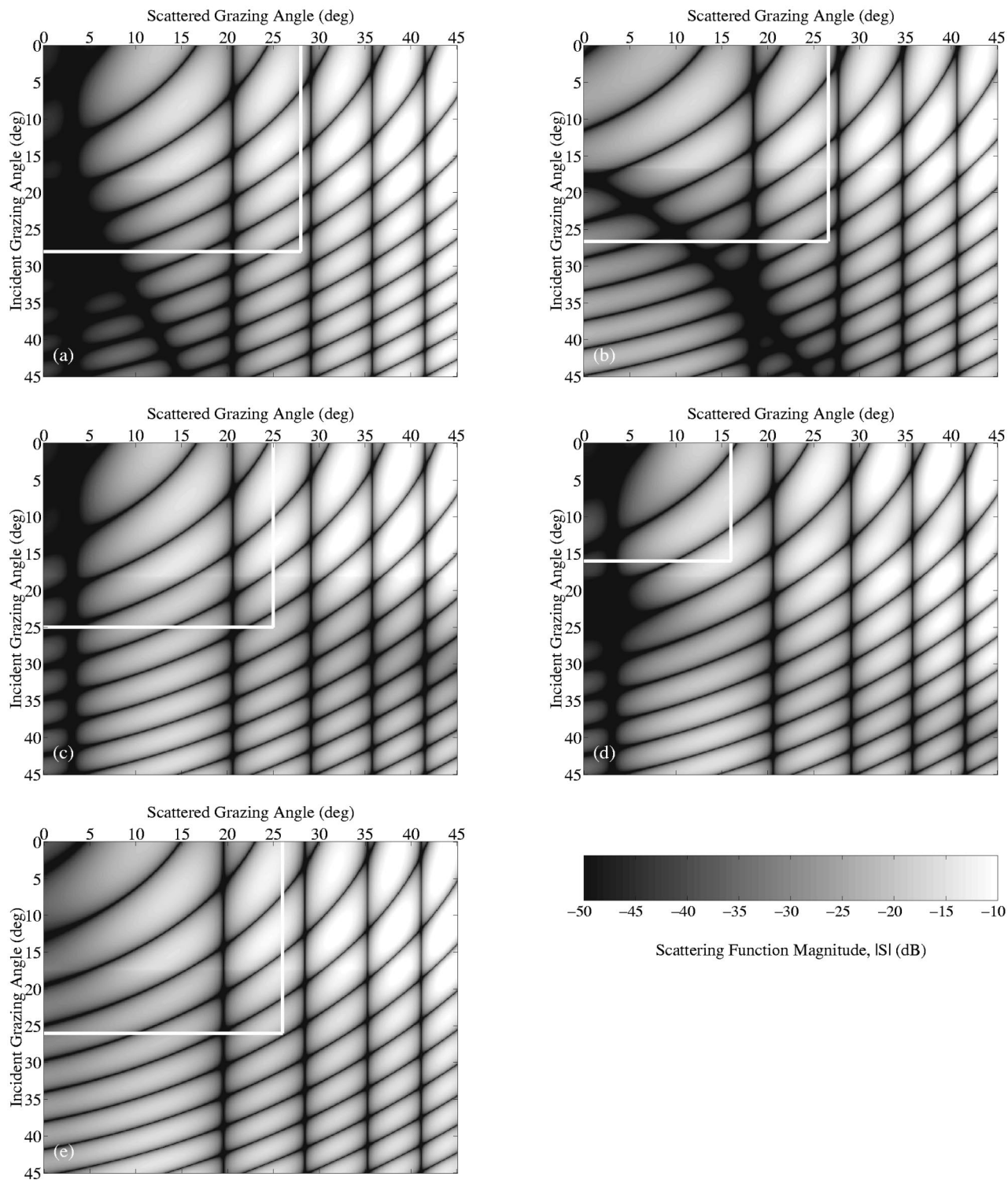


FIG. 10. Magnitudes of the coherent scattering functions $|S(\alpha, \beta = \pi, \alpha_i, \beta_i = 0)|$, i.e., $20 \log |S|$ dB, for the $100 \times 100\text{-m}^2$ seafloor and subseafloor riverbank features at inclination $\chi = 10$ degrees of Fig. 6 over bistatic horizontal grazing angle $\pi/2 - \alpha_i$ for the incident and $\alpha - \pi/2$ for the scattered wave, as appropriate for backscatter in a waveguide. The boxes include all modes n where $0.5 \text{ rad/km} > \text{Im}\{\xi_n\}$. This includes all and only trapped modes for the Pekeris waveguide scenario of Fig. 6(a). (a) Reflection coefficient for water to sand is used for scenario of Fig. 6(a). (b) Reflection coefficient of silt to sand is used for scenario of Fig. 6(c). (c) Double reflection coefficient of water to 2-m silt layer over sand is used for scenario of Fig. 6(b). (d) Double reflection coefficient of water to 5-m silt layer over sand is used for scenario of Fig. 6(b). (e) Double reflection coefficient of light silt to 1-m silt layer over sand is used for scenario of Fig. 6(d).

for riverbank returns and $10 \log \bar{V}_B$ for diffuse reverberation.

For the single-layered bottom scenarios of Figs. 6(b) and (c), returns from both the seafloor riverbank and subseafloor riverbank features can stand well above diffuse seafloor re-

verberation from the silt-over-sand bottom when the riverbank is treated as a coherent scatterer and the silt layer is 2 m or $\frac{2}{3}$ of a wavelength, as shown in Figs. 8(a) and (b). The subseafloor riverbank and seafloor riverbank return echoes at

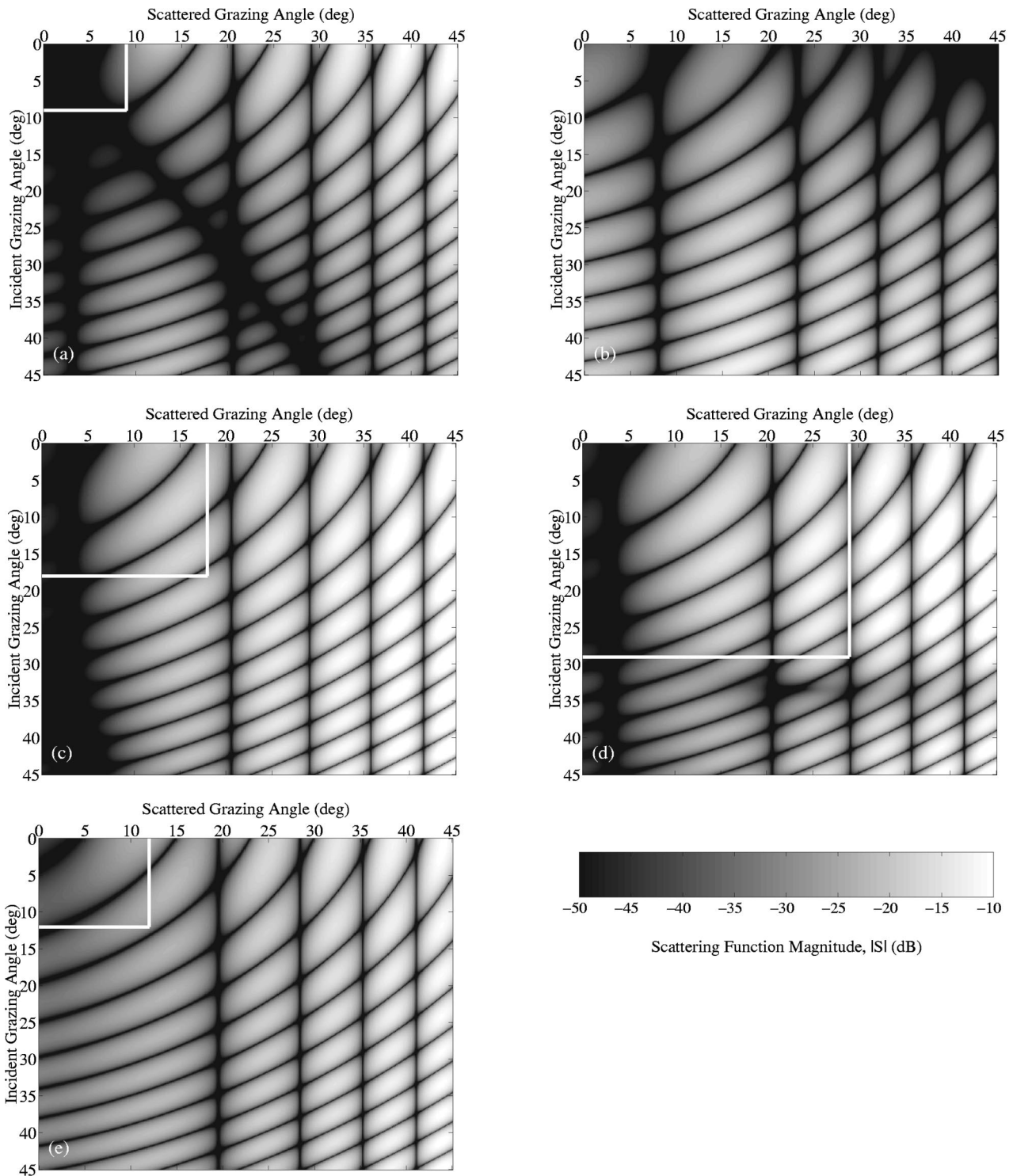


FIG. 11. Same as Fig. 10 except (a) reflection coefficient for water to silt is used for scenario of Fig. 6(a). (b) Reflection coefficient of sand to silt is used for scenario of Fig. 6(c). (c) Double reflection coefficient of water to 2-m sand layer over silt is used for scenario of Fig. 6(b). (d) Double reflection coefficient of water to 5-m sand layer over silt is used for scenario of Fig. 6(b). (e) Double reflection coefficient of light silt to 1-m sand layer over silt is used for scenario of Fig. 6(d).

similar levels within roughly 5 km, where both features typically stand above the diffuse seafloor reverberation by roughly 10 dB, which exceeds the 5.6-dB standard deviation. The prominence of the subseafloor riverbank returns follows from the greater impedance mismatch between the silt–sand interface than the water–silt interface incorporated in the riverbank scatter function. Beyond roughly 5 km, the subsea-

floor feature has returns that fall off more rapidly than those of the seafloor feature. This follows from the stripping of higher-order modes that propagate with high attenuation in the silt layer. Coherent returns from the riverbank arise because of its finite extent. Since the riverbank is modeled as a smooth flat surface, scattering is greatest in the specular direction and falls off in other directions in a manner similar to

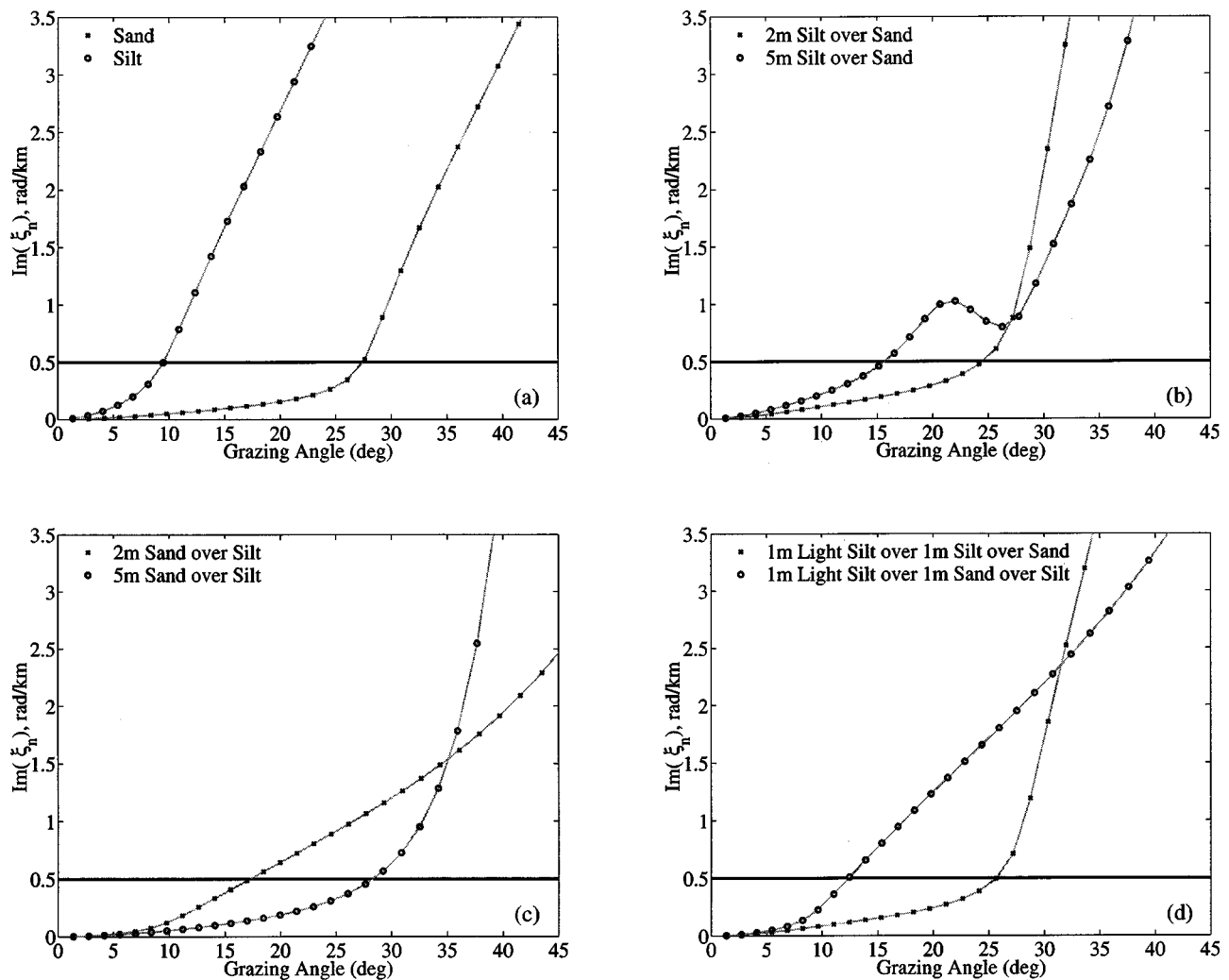


FIG. 12. The horizontal wave number's imaginary component $\text{Im}\{\xi_n\}$ is plotted as a function of horizontal grazing angle, $|\pi/2 - \alpha_i|$, for the various waveguides considered. Proper modes occur in Pekeris below the critical angle for $0.5 \text{ rad/km} > \text{Im}\{-\xi_n\}$. (a) Pekeris with sand bottom and Pekeris with silt bottom. (b) Constant water column sound speed of 1500 m/s over $h_1=2\text{-m}$ and $h_1=5\text{-m}$ silt layer over sand half-space. (c) Constant water column sound speed of 1500 m/s over $h_1=2\text{-m}$ and $h_1=5\text{-m}$ sand layer over silt half-space. (d) Constant water column sound speed of 1500 m/s over 1-m light silt layer over 1-m silt layer over sand half-space and constant water column sound speed of 1500 m/s over 1-m light silt layer over 1-m sand layer over silt half-space.

the sidelobes of a phased array's beampattern. In backscatter, for the given geometry, the riverbank returns increase in intensity with the square of its length, or cross-range extent. Longer riverbanks that fit within the sonar resolution footprint then yield significantly larger returns as a consequence of the coherent scattering assumption, and may stand well above diffuse seafloor reverberation beyond 10 km. Returns from such extended riverbanks, however, rapidly become more of a challenge to model since the near field moves out in range from the feature with the square of its length. As the range extent of the riverbank increases, the coherent area increases but the side lobe level decreases for the present geometry, rendering the effect on the backscattered field less apparent than in cross-range augmentation.

When the thickness of the silt layer is increased to 5 m, or one wavelength, returns from the subseafloor riverbank features are somewhat reduced, as shown in Fig. 8(c), and again only stand above diffuse seafloor reverberation within roughly 5 km. This follows from a related increase in the stripping of the higher-order modes that have propagating components in the sediment layer since the sediment layer

has much higher attenuation than the water column. The seafloor riverbank feature stands above diffuse seafloor reverberation beyond 20 km but rarely in excess of the Gaussian field standard deviation of 5.6 dB.

When the sediment layer is composed of sand and the half-space below is made of silt, the situation changes drastically, as shown in Figs. 8(d) and (e). Returns from the subseafloor riverbank no longer stand above diffuse seafloor reverberation beyond 2 km because in the sand layer, which is much faster than the water column and silt half-space, the trapped modes become evanescent. Seafloor riverbank returns stand well above diffuse seafloor reverberation, occasionally by 10 dB or more, even beyond 20 km for both the 2- and 5-m-thick sand layers, as expected given the large impedance contrast between water and sand. Older seafloor features, in fact, are more likely to be composed of consolidated material such as sand or limestone since such materials are better able to withstand erosion. Steeper seafloor features that are common in many continental shelves, such as glacier and iceberg scours, can yield even higher returns.

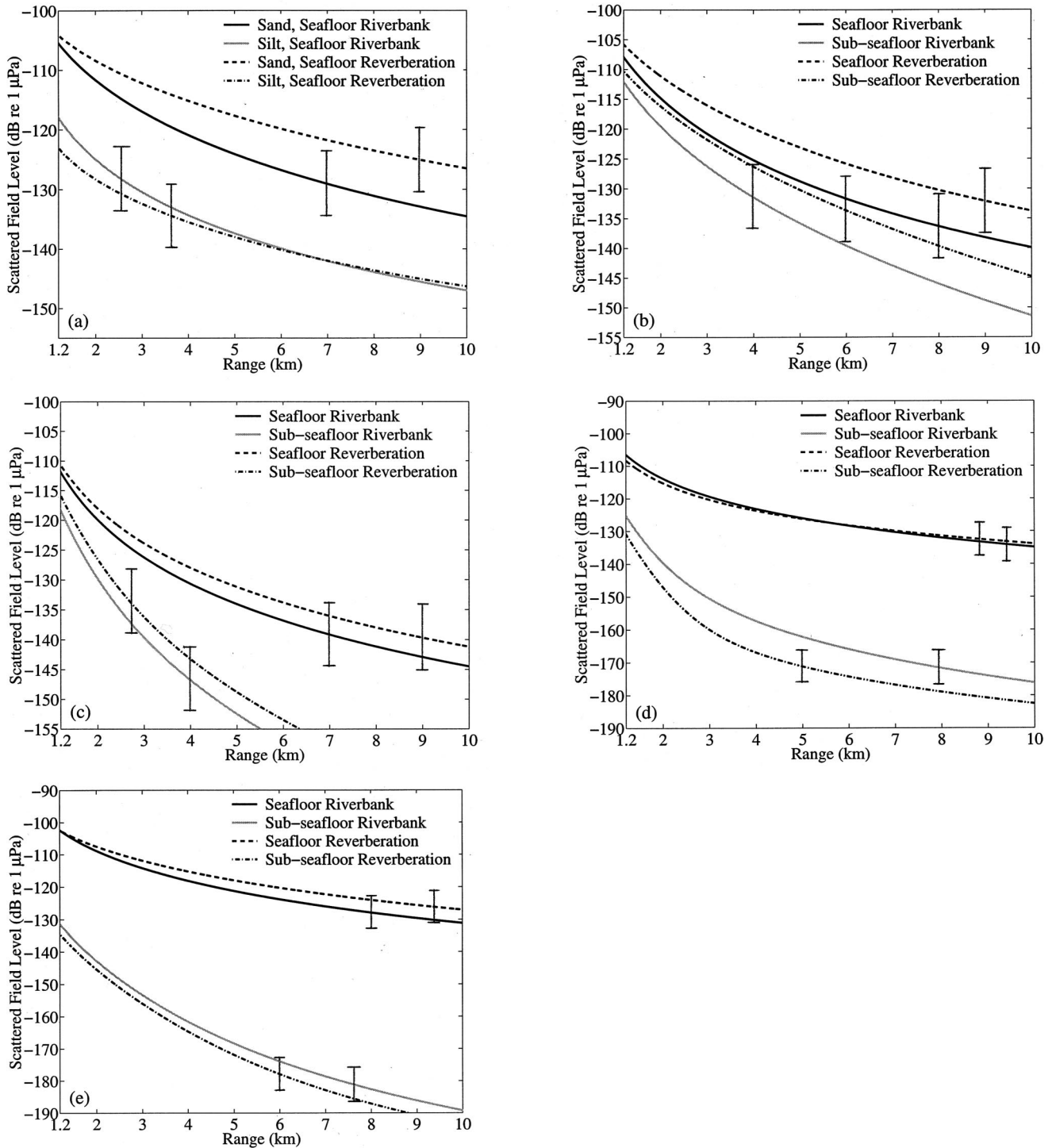


FIG. 13. Same as Figs. 7 and 8 except the Lambert–Mackenzie model is used to model scattering from inclined riverbank features. (a) Seafloor riverbank over sand and silt half-spaces. (b) Seafloor and subseafloor riverbank scattering with the upper sediment layer composed of silt with $h_1=2$ m and the lower sediment half-space composed of sand. (c) Same as (b) except $h_1=5$ m. (d) Seafloor and subseafloor riverbank scattering with the upper sediment layer composed of sand with $h_1=2$ m and the lower sediment half-space composed of silt. (e) Same as (d) except $h_1=5$ m.

For the two-layered bottom of Fig. 6(d), the subseafloor riverbank returns stand roughly 10 dB above diffuse seafloor reverberation out to roughly 10 km for a 1-m light-silt layer over a 1-m silt layer over a sand half-space, as shown in Fig. 9(a). The double layer reflection coefficient from the light-silt to silt to sand interfaces leads to the increased prominence of the subseafloor riverbank returns, compared with those obtained with the single-layer reflection coefficient of

Figs. 8(a)–(e). When the layering is altered to 1-m light-silt over sand over a silt half-space, returns from the subseafloor riverbank feature only stand above diffuse seafloor reverberation within roughly 5 km. This indicates that sediment stratification of the geomorphic feature can weigh in heavily in fixing its scattering amplitude.

The effect of bottom layering on the coherent scattering function of the inclined seafloor and subseafloor riverbank

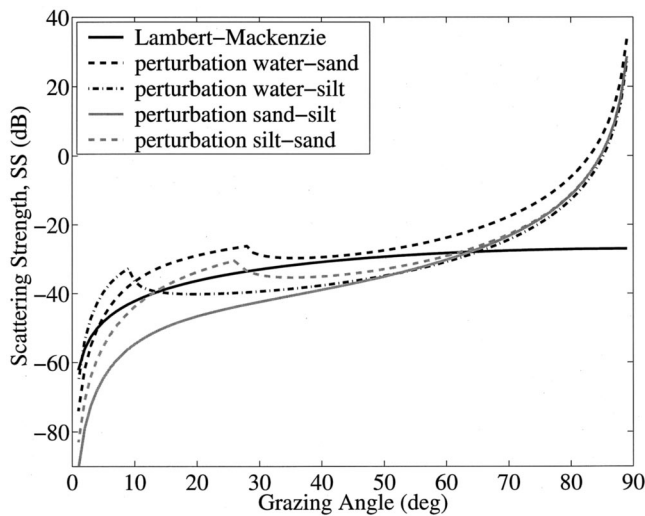


FIG. 14. Scattering strength $SS(\theta = \pi - \theta_i, \phi = 0; \theta_i, \phi_i = \pi)$ in free-space backscatter as a function of surface grazing angle $|\pi/2 - \theta_i|$ for a diffusely scattering surface obeying Lambert-Mackenzie and first-order perturbation theory scattering laws. The first-order perturbation theory curves are for cases where the plane wave is incident from an upper to a lower medium, where the upper and lower media can be water, sand, or silt.

features of Fig. 6 is illustrated in Figs. 10 and 11 as a function of horizontal grazing angle, $\pi/2 - \alpha_i$ for the incident and $\alpha - \pi/2$ for the scattered wave, at fixed incident and scattered azimuths, $\beta_i = 0, \beta = \pi$, as is appropriate to backscatter in a waveguide. The trapped modes for the Pekeris waveguide scenarios, Fig. 10(a) for a sand bottom and Fig. 11(a) for a silt bottom, have incident and scattered elevation angles that lie within the boxes shown, the dimensions of which correspond to the respective bottom critical angle. The boxes include all modes n where $0.5 \text{ rad/km} > \text{Im}\{\xi_n\}$. This includes all and only trapped modes for the Pekeris waveguide scenario of Fig. 6(a). The latter criterion is used to segment modes that dominate the incident propagation by similar boxes for the more complicated layered bottom cases illustrated in Figs. 10 and 11. The value $\text{Im}\{\xi_n\}$ is plotted as a function of equivalent modal angle α in Fig. 12 for the various waveguides considered. This makes it possible to see how the scattering functions of Figs. 10 and 11 are discretely sampled in the waveguide scattering theory defined by Eq. (1) and to estimate the attenuation of a given modal component as a function of range. Inspection of Figs. 10 and 11 reveals that seafloor and subseafloor riverbank features that backscatter most prominently in Figs. 7–9 have scatter functions with relatively large amplitudes at the equivalent angles of the propagating modes. While modes propagating at steeper angles suffer greater attenuation, as indicated in Fig. 12, these same modes are scattered much more efficiently by the slightly inclined riverbank features as indicated in Figs. 10–11, so that there is some balancing between the two effects that is unique to waveguide scattering. Higher-order modes, with elevation angles less than 45 degrees where 0 degrees points downward, however, contribute negligibly to the field scattered from the riverbank features for the ranges and features investigated in the present article.

When the riverbank is treated as an incoherent scatterer with the Lambert-Mackenzie model of Eq. (41), returns

from both the $100 \times 100\text{-m}^2$ seafloor and subseafloor riverbank features at 10 degrees inclination never stand above diffuse seafloor reverberation by more than a fraction of the expected 5.6-dB standard deviation, as shown in Fig. 13. Riverbank returns are again in decibels, i.e., 10 times the log of the covariance given in Eq. (41). This is still the case for the ranges shown in Fig. 13, except for the 2-m sand layer, even if the riverbank feature is extended laterally to fill the entire cross-range width of the system resolution footprint, as can be readily checked by noting that diffuse reverberation accrues in direct proportion to the area of the scattering patch. For the 2-m sand layer, the seafloor riverbank can have returns that exceed the diffuse reverberation background by more than 5.6 dB if it fills the entire resolution footprint in cross-range.

Diffuse subbottom reverberation, shown in Fig. 13, always returns at a lower level than diffuse seafloor reverberation if the same empirical Lambert-Mackenzie incoherent scattering law is used. This comparison highlights the differences in propagation to and from the seafloor and subbottom interfaces since the scattering function is held fixed. The comparison may be purely academic, however, because the Lambert-Mackenzie law serves as an empirical catch-all that describes the entire seabed scattering process and so already incorporates the effect of bottom layering and volume scattering in some average sense. There is, in other words, no reason to believe that scattering from the different interfaces can be modeled with exactly the same albedo and scattering law.

Perturbation theory offers a more fundamental approach to modeling rough surface scattering that can also be used to investigate potential mechanisms for geological clutter. While the impedance contrast at the scattering interface is fully accounted for in the perturbation theory formulation, additional parameters describing the roughness spectrum must be known. The perturbation theory formulation described in Sec. III D is used with the spectral strength and power law parameters $w_2 = 0.04/(2\pi)$ and $\gamma = 4.0$, yielding frequency-independent scattering, following Essen.³³ These values are not based on physical measurements, since none are presently available in the present frequency range, but rather have been chosen so that the scattering strength that perturbation theory yields is near that of the empirical Lambert-Mackenzie model for the various single and multiple reflection interfaces considered here, as shown in Fig. 14. In all curves where scattering arises from a wave incident from a slower medium, a discontinuity in slope is found at the critical angle. Beyond this a significant reduction in scattering occurs until roughly 45 degrees where shallow angle assumptions of first-order perturbation theory are no longer valid for the given surface roughness parameters, and the curves increase dramatically in an unphysical manner. Differences in the perturbation theory curves away from the critical angles arise principally from the impedance contrasts between the media considered. An exception occurs for fast sand over slow silt where no critical angle exists and transmission into the silt is significant even at very shallow angles, where low level scattering results.

The effect of scattering and reflection from multiple lay-

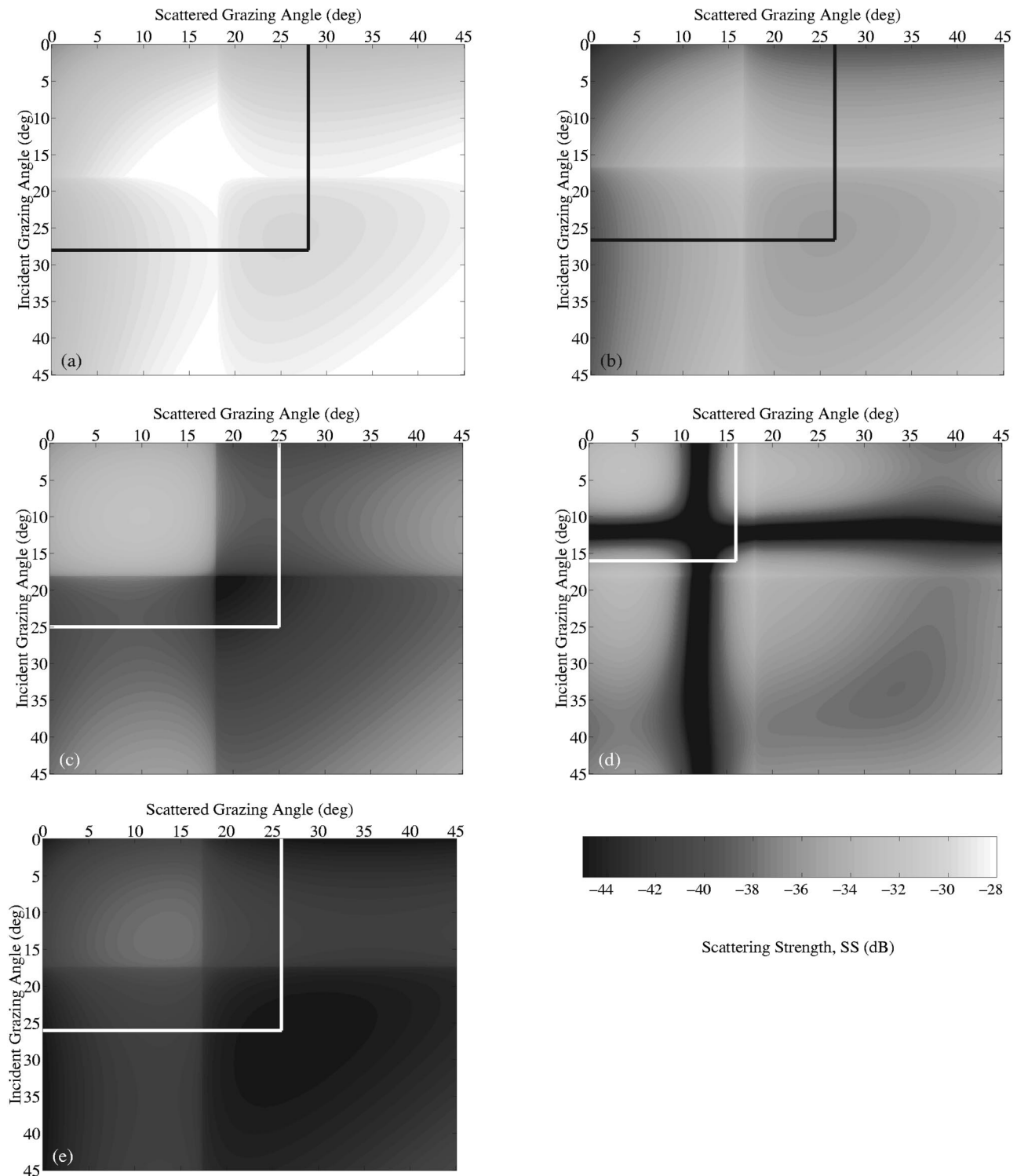


FIG. 15. Scattering strength $SS(\alpha, \beta = \pi, \alpha_i, \beta_i = 0)$, based on first-order perturbation theory for the seafloor and subseafloor riverbank features at inclination $\chi = 10$ degrees of Fig. 6 over bistatic horizontal grazing angle $\pi/2 - \alpha_i$ for incident waves and $\alpha - \pi/2$ for scattered waves, as appropriate to backscatter in a waveguide. The boxes include all modes n where $0.5 \text{ rad/km} > \text{Im}\{\xi_n\}$. This includes all and only trapped modes for the Pekeris waveguide scenario of Fig. 6(a). (a) Reflection coefficient for water to sand is used for scenario of Fig. 6(a). (b) Reflection coefficient of silt to sand is used for scenario of Fig. 6(c). (c) Double reflection coefficient of water to 2-m silt layer over sand is used for scenario of Fig. 6(b). (d) Double reflection coefficient of water to 5-m silt layer over sand is used for scenario of Fig. 6(b). (e) Double reflection coefficient of light slit to 1-m silt layer over sand is used for scenario of Fig. 6(d).

ers can be significant as shown in Figs. 15 and 16 for an inclined riverbank surface and Figs. 17 and 18 for general uninclined seafloor, where the perturbation theory scattering strength is presented for the bistatic scattering scenario rel-

evant to backscatter in a waveguide, as was done in Figs. 10 and 11 for the coherent scatter function.

Empirical values for the spectral strength and power law parameters of first-order perturbation theory have been ob-

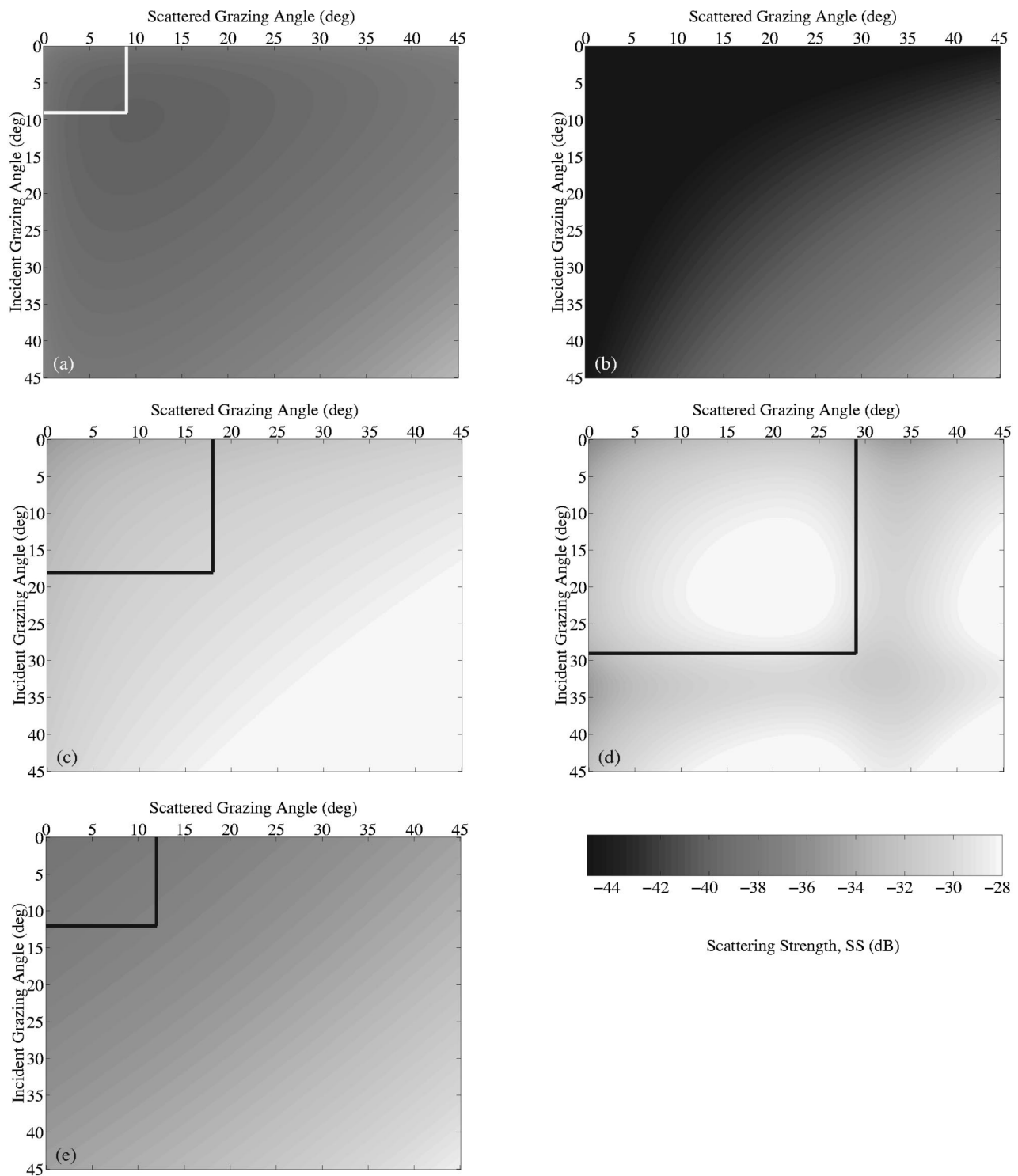


FIG. 16. Same as Fig. 15 except (a) reflection coefficient for water to silt is used for scenario of Fig. 6(a). (b) Reflection coefficient of sand to silt is used for scenario of Fig. 6(c). (c) Double reflection coefficient of water to 2-m sand layer over silt is used for scenario of Fig. 6(b). (d) Double reflection coefficient of water to 5-m sand layer over silt is used for scenario of Fig. 6(b). (e) Double reflection coefficient of light silt to 1-m sand layer over silt is used for scenario of Fig. 6(d).

tained for various seafloor types by Jackson³⁴ over the short spatial scales relevant to the analysis of high-frequency scattering in the ten kilohertz range and beyond, where this author has shown perturbation theory to match experimental data well. When these same values are used at low frequency, specifically $f = 300$ Hz, the resulting scattering law falls more than an order of magnitude below the empirical

Lambert–Mackenzie curve shown in Fig. 14. Unrealistically high roughness values for the spectral strength, as obtained for rough, rocky surfaces in the high-frequency analysis of Ref. 34, are necessary for first-order perturbation theory to match the empirical seafloor scattering strength curve of Mackenzie in the low-frequency regime of interest here. Since the Mackenzie curve summarizes the entire seafloor

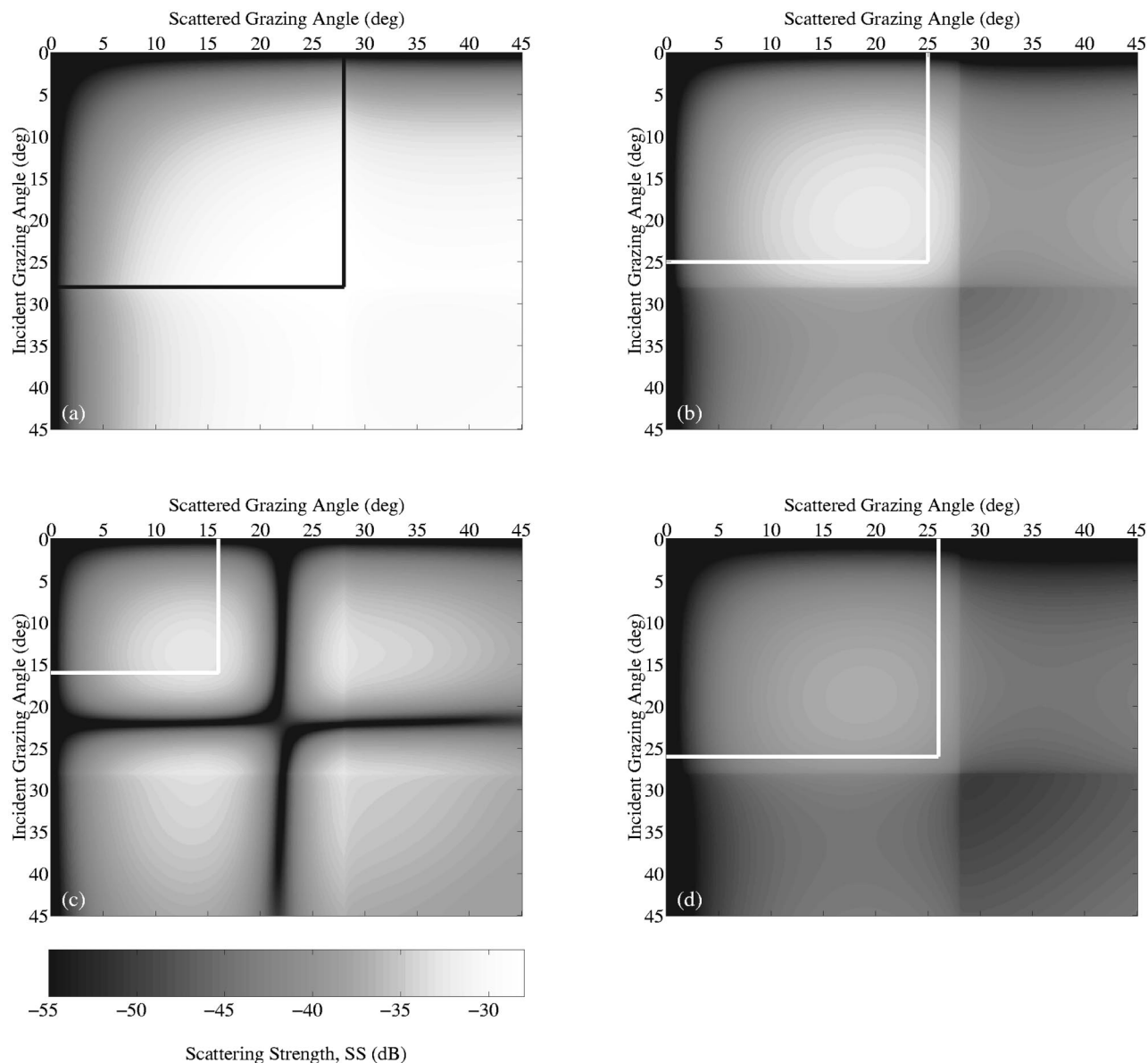


FIG. 17. Scattering strength $SS(\alpha, \beta=\pi, \alpha_i, \beta_i=0)$ based on first-order perturbation theory for level seafloor, $\chi=0$ degrees, over bistatic horizontal grazing angle $\pi/2 - \alpha_i$ for the incident wave and $\alpha - \pi/2$ for the scattered wave, as appropriate to backscatter in a waveguide. The boxes include all modes n where $0.5 > \text{Im}\{\xi_n\}$. This includes all and only trapped modes for the Pekeris waveguide scenario of Fig. 6(a). (a) Reflection coefficient for water over sand is used. (b) Double reflection coefficient of water over 2-m silt over sand is used. (c) Double reflection coefficient of water over 5-m silt layer over sand is used. (d) Triple reflection coefficient of water over 1-m light silt layer over 1-m silt layer over sand is used.

scattering process, and is not limited to interface scattering or the more restrictive type of interface scattering described by first-order perturbation theory, it is reasonable to conclude that either the assumptions of first-order perturbation theory are inadequate to properly model seafloor scattering at low frequency, a significantly different set of spectral strength and power law parameters must characterize seafloor interface scattering at low frequency, or a more sophisticated modeling of the seabed layering and sound speed gradients is necessary. It is also possible that scattering from volume heterogeneities may yield significant reverberation. This is most likely to be the case where a propagating, rather than evanescent, component of the modal spectrum exists in the layer where the volume heterogeneities are present.

When the riverbank feature is treated as an incoherent

scatterer using first-order perturbation theory, as in Figs. 19 and 20, only seafloor riverbank returns from a single sand layer can stand above diffuse seafloor reverberation by more than 5.6 dB, and this only occurs when the riverbank feature is extended laterally to fill the entire cross-range extent of the system resolution footprint. Returns from the subseafloor riverbank only stand above diffuse seafloor reverberation by more than 5.6 dB for the two-layered bottom in the light-silt over sand over silt scenario, and this only occurs if the feature is extended to fill the resolution footprint.

Comparison of Figs. 7 and 9 and Fig. 13 shows that coherent returns greatly outweigh incoherent returns from the riverbank feature. This finding is advantageous since only deterministic physical and geometrical parameters of the seafloor are necessary in the coherent model, whereas

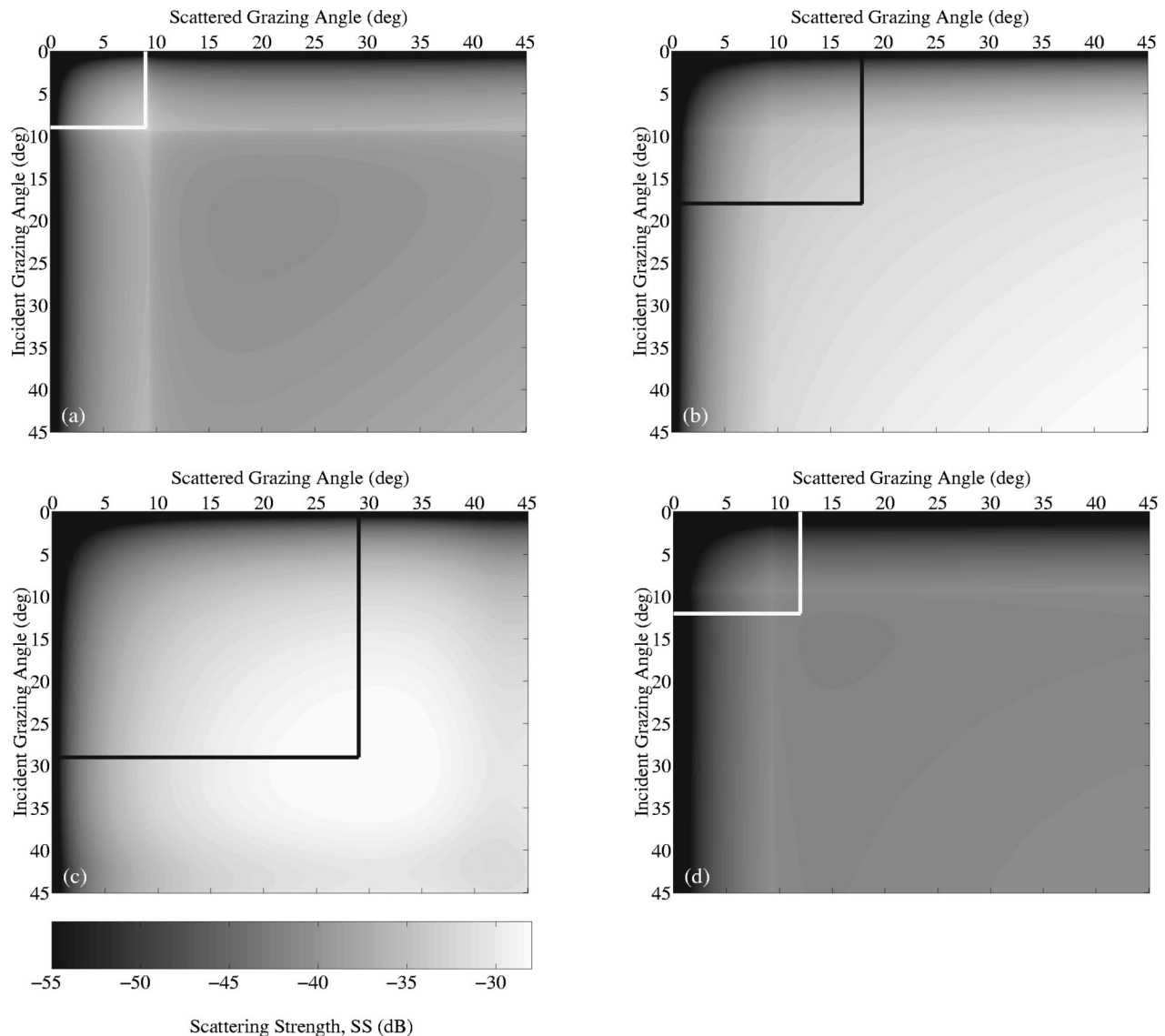


FIG. 18. Same as Fig. 17 except (a) reflection coefficient for water over silt is used. (b) Double reflection coefficient of water over 2-m sand over silt is used. (c) Double reflection coefficient of water over 5-m sand layer over silt is used. (d) Triple reflection coefficient of water over 1-m light silt layer over 1-m sand layer over silt is used.

either empirical data or a stochastic representation of the seafloor is necessary in the incoherent model. The environmental description necessary for the coherent model is then easier to obtain and rests on far fewer supporting assumptions than the incoherent one.

V. CONCLUSIONS

One of the greatest challenges to active sonar operations in shallow water arises when echo returns from the intended target become indistinguishable from reverberation returned by the waveguide boundaries and volume. To determine conditions in which a typical low-frequency active sonar system may operate effectively in a shallow water waveguide, a unified model for submerged object scattering and reverberation is developed. The approach is to use a waveguide scattering model that follows directly from Green's theorem but that takes advantage of simplifying single-scatter and far-field approximations that apply to a wide variety of problems where

the source and receiver are distant from the target. To treat reverberation from randomly rough boundaries and stochastic volume inhomogeneities, the waveguide scattering model is generalized to include stochastic targets. Analytic expressions for the spatial covariance of the field scattered from a stochastic target are then obtained in terms of the waveguide Green's function and the covariance of the target's plane wave scatter function. This makes the formulation amenable to a wide variety of approaches for computing a stochastic target's scatter function. For diffuse seafloor reverberation, two approaches are adopted, an empirical one of Lambert and Mackenzie and a fundamental one based on first-order perturbation theory. It is most convenient to describe the diffuse component of distant seafloor reverberation with a modal formulation since the modes comprise the statistical entities of the field that the scattering surface may decorrelate.

Since reverberation is measured in time but the waveguide scattering formulation is for harmonic field compo-

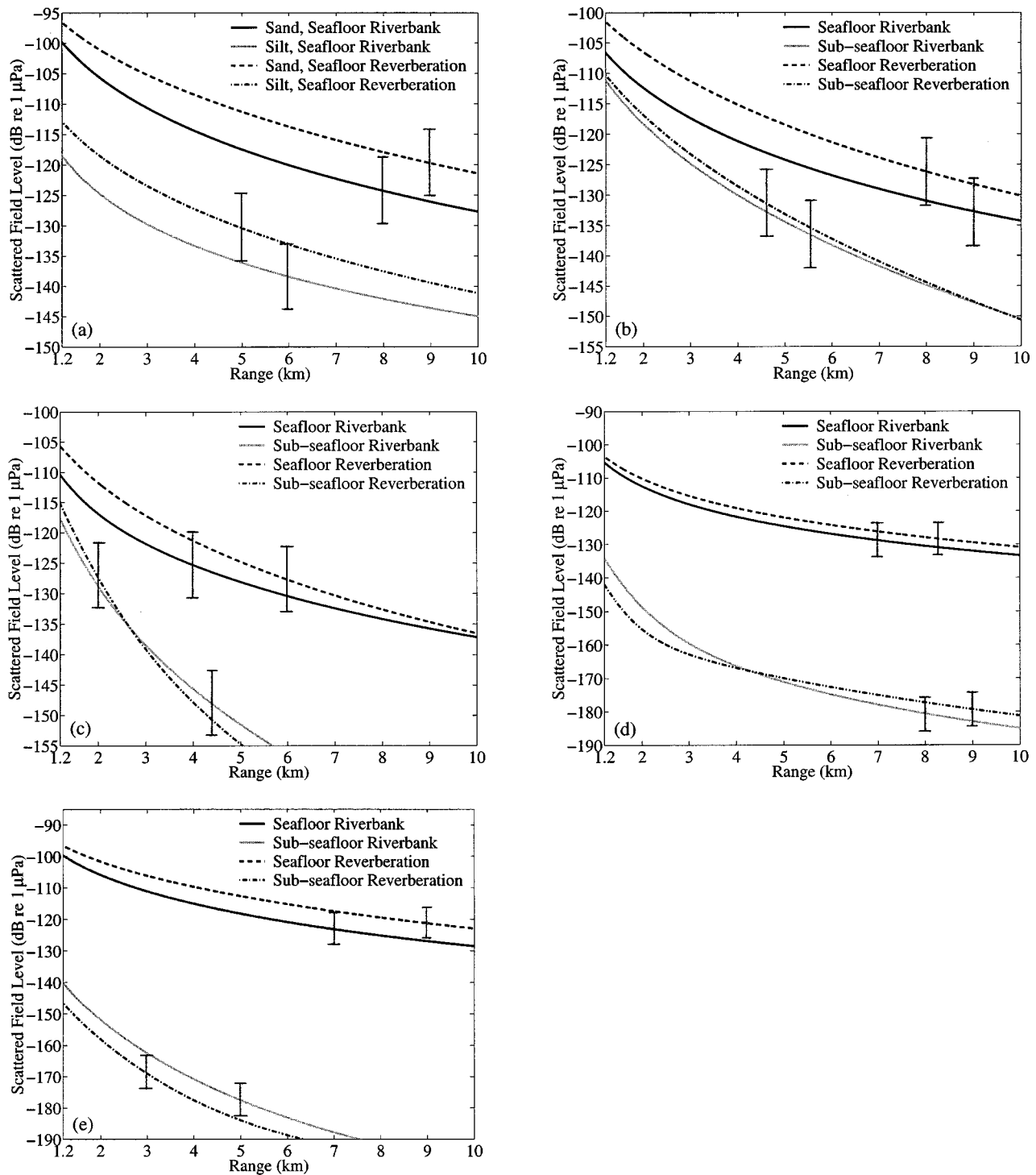


FIG. 19. Same as Figs. 7 and 8 except first-order perturbation theory is used to model scattering from the inclined riverbank features. (a) Seafloor riverbank over sand and silt half-spaces. (b) Seafloor and subseafloor riverbank scattering with the upper sediment layer composed of silt with $h_1=2$ m and the lower sediment half-space composed of sand. (c) Same as (b) except $h_1=5$ m. (d) Seafloor and subseafloor riverbank scattering with the upper sediment layer composed of sand with $h_1=2$ m and the lower sediment half-space composed of silt. (e) Same as (d) except $h_1=5$ m.

nents, the time dependence of the field scattered by a distant object from a source of arbitrary time dependence is derived analytically using the saddle point method. The resulting expression is given in terms of modal group velocities, the frequencies of which vary as a function of time and source, receiver, and target position. A simpler analytic approach involving Parseval's theorem can be applied when the integration time of the measurement system is sufficiently long

to include the dominant energy returned from the target or scattering patch. This approach is used in the illustrative examples. A viewer-oriented reference frame is then adopted, translating from the traditional target-oriented frame of waveguide scatter theory, to incorporate the continuous distribution of scatterers encountered in waveguide boundary and volume reverberation. This enables analytic expressions to be developed for the reverberant field returned bistatically

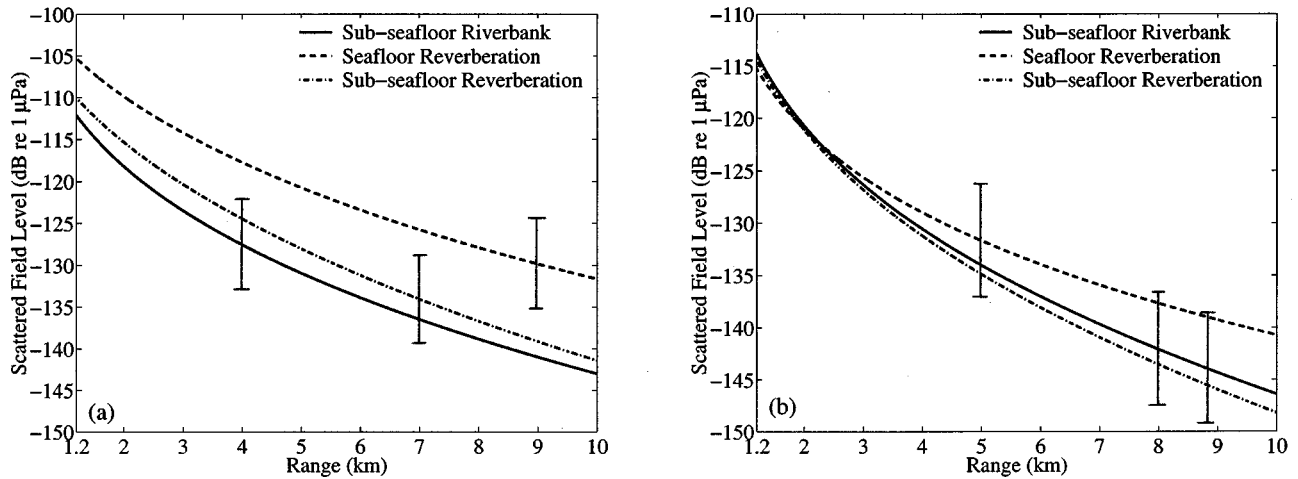


FIG. 20. Same as Fig. 9 except first-order perturbation theory is used to model scattering from the inclined subseafloor riverbank for the two-layer bottom scenario of Fig. 6(d). (a) Sediment is comprised of light silt layer of $h_1 = 1$ -m thickness over a silt layer of $h_1 = 1$ -m thickness over a sand half-space. Diffuse riverbank scattering is from the double interface of light silt to silt to sand. (b) Sediment is comprised of light silt layer of $h_1 = 1$ -m thickness over a sand layer of $h_2 = 1$ -m thickness over a silt half-space. Diffuse riverbank scattering is from the double interface of light silt to sand to silt.

from seafloor within the resolution footprint of a typical active sonar system after narrow-band beamforming with a horizontal array.

The unified model is used to investigate typical low-frequency active detection scenarios in shallow water. Sample calculations for finite-duration cw source signals indicate that the maximum range at which echo returns from a submerged target stand unambiguously above diffuse seafloor reverberation is highly dependent upon the water column and sediment stratification, as well as the receiving array aperture, source, receiver, and target location, and the scattering properties of the target and seafloor.

The model is also applied to determine conditions in which discrete morphological features of the seafloor and subseafloor return echoes that stand prominently above diffuse seafloor reverberation. Simulations for finite-duration cw source signals indicate that typical seafloor and subseafloor riverbank features, ubiquitously found throughout continental shelf waters, can return echoes that stand significantly above the diffuse component of seafloor reverberation in the operational ranges of typical low-frequency active sonar systems. This finding is significant since returns from these discrete features can be confused with returns from an intended submerged target. The relative prominence of this kind of geological clutter is highly dependent on the waveguide properties, measurement geometry, and scattering characteristics of the geological feature and surrounding seafloor. The finding that subseafloor features can cause significant clutter is particularly troubling for active sonar operations because it greatly increases the environmental characterization necessary to make accurate predictions of the expected clutter. The coherent component of the field scattered from the riverbank features examined, arising from the features' finite size, is found to far outweigh the diffuse component arising from random roughness of the features. The methods and findings of this article are presently being used to help design a number of field experiments to investigate the physical mechanisms that lead to geological clutter

in the output of active sonar systems operated in shallow water.

ACKNOWLEDGMENTS

The authors would like to thank the Office of Naval Research for financial support and encouragement as well as our colleagues in the Geological Clutter Program for many fruitful discussions.

APPENDIX A: THE PLANE WAVE SCATTER FUNCTION, TARGET STRENGTH, SURFACE SCATTERING STRENGTH, AND GREEN'S THEOREM

Standard parameters used to describe surface and target scattering in ocean acoustics can be traced back to Green's theorem by using some simple approximations involving the plane wave scatter function in free space. To do so, it must be recalled that the harmonic field $\Phi_s(\mathbf{r})$ scattered by an object can be expressed in terms of the medium Green function $G(\mathbf{r}|\mathbf{r}_t)$ and incident field $\Phi_i(\mathbf{r})$ by the Helmholtz-Kirckoff integral equation³⁵

$$\Phi_s(\mathbf{r}) = - \int_{A_t} \int [\Phi_i(\mathbf{r}_t) + \Phi_s(\mathbf{r}_t)] \frac{\partial G(\mathbf{r}|\mathbf{r}_t)}{\partial n_t} - G(\mathbf{r}|\mathbf{r}_t) \frac{\partial}{\partial n_t} [\Phi_i(\mathbf{r}_t) + \Phi_s(\mathbf{r}_t)] dA_t, \quad (A1)$$

a form of Green's theorem, where $G(\mathbf{r}|\mathbf{r}_t)$ and $\Phi_i(\mathbf{r})$ each satisfy the Helmholtz equation, driven by a source at angular frequency $\omega = 2\pi f$. The area integral encloses the scatterer and the surface normal points into the enclosed volume.

Consider, first, the problem of a plane wave

$$\Phi_i(\mathbf{r}_t) = e^{ikr_t \eta(\theta_i, \phi_i)}, \quad (A2)$$

incident on an object in free space traveling in the direction (θ_i, ϕ_i) where, for example,

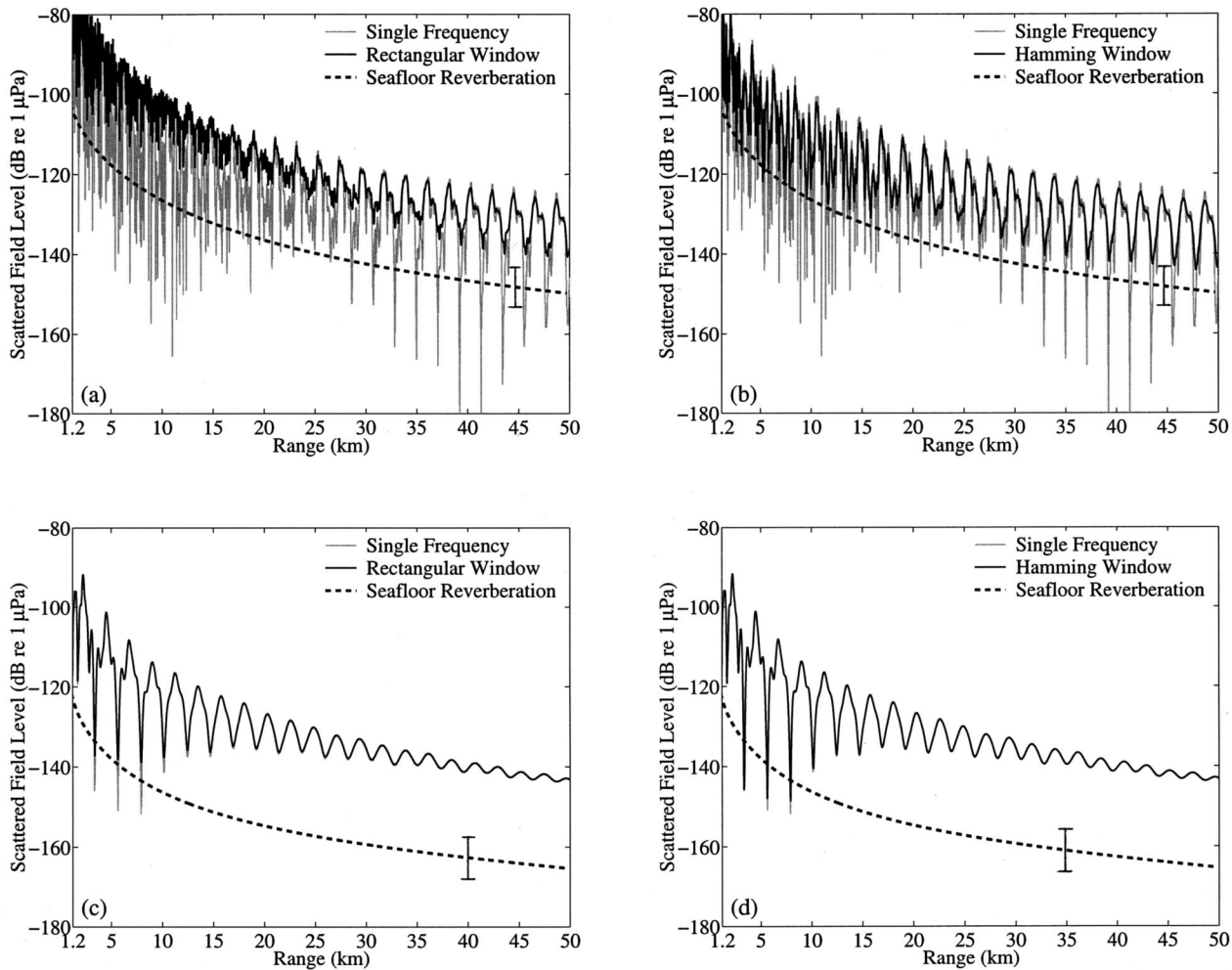


FIG. B1. A comparison of scattering using the single frequency approximation versus the full bandwidth of the given window function. Reverberation calculated using the single frequency approximation is indistinguishable from that calculated with the full bandwidth. (a) Same as Fig. 3(a) for sphere in waveguide with reverb except only the sand bottom case is shown. Single frequency approximation is compared to rectangular window. (b) Same as (a) except the Hamming window is used instead of the rectangular window. (c) Same as (a) except only the silt bottom case is shown. (d) Same as (c) except the Hamming window is used instead of the rectangular window.

$$\eta(\theta_i, \phi_i) = \cos \theta_i \cos \theta_t + \sin \theta_i \sin \theta_t \cos(\phi_i - \phi_t). \quad (\text{A3})$$

The Green function is

$$G(\mathbf{r}|\mathbf{r}_t) = \frac{1}{4\pi} \frac{e^{ik|\mathbf{r}-\mathbf{r}_t|}}{|\mathbf{r}-\mathbf{r}_t|} \approx \frac{1}{4\pi} \frac{e^{ik[r-r_t\eta(\theta, \phi)]}}{r}, \quad (\text{A4})$$

where the last approximation is for a receiver so far from the object that $r \gg r_t$. By application of Green's theorem, the scattered field at this distant receiver then can be written as

$$\Phi_s(\mathbf{r}) \approx -\frac{e^{ikr}}{4\pi r} \iint_{A_t} [e^{ikr_t\eta(\theta_i, \phi_i)} + \Phi_s(\mathbf{r}_t)] \frac{\partial}{\partial n_t} e^{-ikr_t\eta(\theta, \phi)} - e^{-ikr_t\eta(\theta, \phi)} \frac{\partial}{\partial n_t} [e^{ikr_t\eta(\theta_i, \phi_i)} + \Phi_s(\mathbf{r}_t)] dA_t. \quad (\text{A5})$$

By the definition of the plane wave scatter function $S(\theta, \phi; \theta_i, \phi_i)$, however, it can also be written as

$$\Phi_s(\mathbf{r}) \approx S(\theta, \phi; \theta_i, \phi_i) \frac{e^{ikr}}{kr}, \quad (\text{A6})$$

in an object-centered coordinate system, which leads to the equality

$$S(\theta, \phi; \theta_i, \phi_i) = -\frac{k}{4\pi} \iint_{A_t} [e^{ikr_t\eta(\theta_i, \phi_i)} + \Phi_s(\mathbf{r}_t)] \frac{\partial}{\partial n_t} e^{-ikr_t\eta(\theta, \phi)} - e^{-ikr_t\eta(\theta, \phi)} \frac{\partial}{\partial n_t} [e^{ikr_t\eta(\theta_i, \phi_i)} + \Phi_s(\mathbf{r}_t)] dA_t, \quad (\text{A7})$$

which relates Eq. (A5) directly to Green's theorem when $r \gg r_t$.

Equation (A5) can be recast as a sonar equation by taking $10 \log$ of the squared magnitude of both sides. In terms of the plane wave scatter function, the resulting target strength of the scatterer is then

$$T = 10 \log \left| \frac{S(\theta, \phi; \theta_i, \phi_i)}{k} \right|^2 \text{ dB re } 1 \text{ m}. \quad (\text{A8})$$

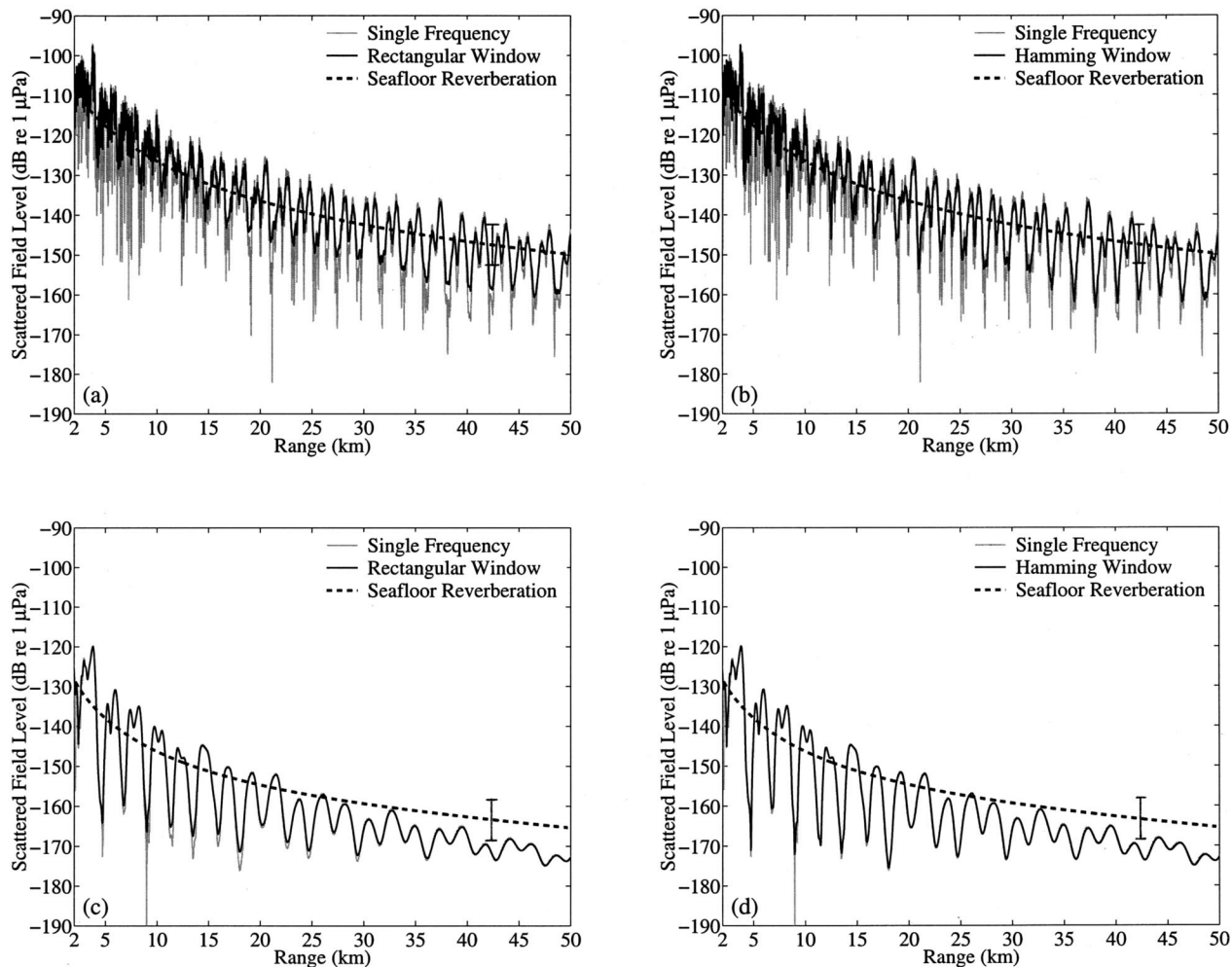


FIG. B2. A comparison of scattering using the single frequency approximation versus the full bandwidth of the given window function. Reverberation calculated using the single frequency approximation is indistinguishable from that calculated with the full bandwidth. (a) Same as Fig. 7(a) for seafloor riverbank with reverb except only the sand bottom case is shown. The single frequency approximation is compared to the rectangular window. (b) Same as (a) except the Hamming window is used instead of the rectangular window. (c) Same as (a) except only the silt bottom case is shown. (d) Same as (c) except the Hamming window is used instead of the rectangular window.

The differential scattering cross section of the target, defined as

$$\sigma = \lim_{r \rightarrow \infty} 4\pi r^2 \frac{|\Phi_s(\mathbf{r})|^2}{|\Phi_i(\mathbf{r})|^2}, \quad (\text{A9})$$

then becomes

$$\sigma(\theta, \phi; \theta_i, \phi_i) = 4\pi \left| \frac{S(\theta, \phi; \theta_i, \phi_i)}{k} \right|^2, \quad (\text{A10})$$

which in the high-frequency limit can be interpreted as the projected area of the target as seen with foreshortening from the combined perspectives of the source and receiver.

If the target is a random patch of rough surface rather than a finite object, Eqs. (A5) and (A6) can still be used so long as far-field conditions hold and $S(\theta, \phi; \theta_i, \phi_i)$ is interpreted as a stochastic parameter. The scattering coefficient of the surface is the expected scattering cross-section per solid angle $\langle \sigma/4\pi \rangle$. This can be written in terms of the bidirectional scattering (reflectance) distribution function²⁹

$f(\theta, \phi; \theta_i, \phi_i)$, a standard empirical descriptor of surface scattering properties in modern radiometry, via

$$\left\langle \frac{\sigma}{4\pi} \right\rangle = f(\theta, \phi; \theta_i, \phi_i) \cos \theta \cos \theta_i \Delta A, \quad (\text{A11})$$

where ΔA is the area of the surface patch. For diffuse scattering that is equal in all directions, the bidirectional scattering distribution function equals the constant ε/π , where ε is the albedo,²⁹ which is unity for a perfect Lambertian surface and roughly $\pi/10^{2.7}$ for a Lambert–Mackenzien surface.⁹ The conventional seafloor scattering strength of ocean acoustics²² is then

$$SS(\theta, \phi; \theta_i, \phi_i) = 10 \log \left\langle \left| \frac{S(\theta, \phi; \theta_i, \phi_i)}{k} \right|^2 \right\rangle - 10 \log \Delta A, \quad (\text{A12})$$

where the first term on the right-hand side can be interpreted as an equivalent target strength for the random scattering patch.

Many surfaces scatter with both a deterministic as well as a fluctuating component. It is conventional to assume that the fluctuating component scatters a zero-mean field. Diffuse scattering surfaces, as described by Lambert's law or first-order perturbation theory, scatter only zero-mean fluctuating fields.

The preceding analysis shows that the standard parameters used to describe surface and target scattering in free space can be traced back to Green's theorem through the plane wave scatter function.

APPENDIX B: SINGLE FREQUENCY APPROXIMATION VERSUS FULL BANDWIDTH IN NARROW-BAND SCATTERING CALCULATIONS

A single frequency approximation is used for all the narrow-band scattering calculations of Sec. IV. The time-averaged, expected mutual intensity of Eq. (35),

$$I(\mathbf{R}, \mathbf{R}_r, \mathbf{R}_0, t) = \frac{1}{T} \int_{-\infty}^{\infty} |Q(f)|^2 \langle |\Phi_s(\mathbf{R}_r - \mathbf{R} | \mathbf{R}_0 - \mathbf{R})|^2 \rangle df, \quad (\text{B1})$$

is approximated as

$$I(\mathbf{R}, \mathbf{R}_r, \mathbf{R}_0, t) \approx \langle |\Phi_s(\mathbf{R}_r - \mathbf{R} | \mathbf{R}_0 - \mathbf{R})|^2 \rangle \times \frac{1}{T} \int_{-\infty}^{\infty} |Q(f)|^2 df, \quad (\text{B2})$$

where $\langle |\Phi_s(\mathbf{R}_r - \mathbf{R} | \mathbf{R}_0 - \mathbf{R})|^2 \rangle$ is calculated at the center frequency f_c of the narrow-band waveform $q(t)$, where $f_c = 300$ Hz for the examples of Sec. IV. In practice, the narrow-band waveform or window function $q(t)$ has a spectrum $Q(f)$ with either a narrow main lobe such as the rectangular window, or a broader main lobe with lower side lobes such as the Bartlett, Hanning, and Hamming windows.³⁶ The window functions are normalized according to

$$\frac{1}{T} \int_{-\infty}^{\infty} |Q(f)|^2 df = 1, \quad (\text{B3})$$

so that the rectangular window, with a main lobe half-power bandwidth of $0.886/T$ and a first side lobe 13.4 dB down peak-to-peak from the main lobe, becomes

$$q(t) = \begin{cases} 1 & \text{for } -T/2 \leq t \leq T/2, \\ 0 & \text{otherwise,} \end{cases} \quad (\text{B4})$$

and the Hamming window, for example with main lobe half-power bandwidth of $1.30/T$ and a first side lobe 42.7 dB down peak-to-peak from the main lobe, becomes

$$q(t) = \begin{cases} \sqrt{1/0.3974} \{0.54 + 0.46 \cos(2\pi t/T)\} & \text{for } -T/2 \leq t \leq T/2, \\ 0 & \text{otherwise,} \end{cases} \quad (\text{B5})$$

where $T = 1/2$ s for the examples of Sec. IV.

For the reverberation calculations of Sec. IV, calculations show that this approximation differs from the full spectral integration by less than 0.1 dB.

As may be expected in the coherent scattering from targets where modal interference is significant, some range-

dependent nulls and valleys in the sound pressure level of the received field found in the single frequency calculation may be partially filled when the full bandwidth is used for the narrow-band waveforms considered. This is exhibited in Figs. B1 and B2 where the filling is shown to be window dependent and more negligible for bottoms that support fewer trapped modes. It is noteworthy that for narrow-band transmissions at the given center frequency and duration, the sphere target may have returns that fall below the expected reverberation level, but the quantity and location of these expected deep "fades" of the target are highly dependent on the window function used.

¹F. Ingenito, "Scattering from an object in a stratified medium," *J. Acoust. Soc. Am.* **82**, 2051–2059 (1987).

²N. C. Makris, F. Ingenito, and W. A. Kuperman, "Detection of a submerged object insonified by surface noise in an ocean waveguide," *J. Acoust. Soc. Am.* **96**, 1703–1724 (1994).

³D. D. Ellis, "A shallow water normal mode reverberation model," *J. Acoust. Soc. Am.* **97**, 2804–2814 (1995).

⁴H. P. Bucker and H. E. Morris, "Normal mode reverberation in channels or ducts," *J. Acoust. Soc. Am.* **44**, 827–828 (1968).

⁵R. H. Zhang and G. L. Jin, "Normal mode theory of the average reverberation intensity in shallow water," *J. Sound Vib.* **119**, 215–223 (1987).

⁶D. M. Fromm, B. J. Orchard, and S. N. Wolf, "Range-dependent normal mode reverberation model for bistatic geometries," in *Ocean Reverberation* (Kluwer, Dordrecht, The Netherlands, 1993), pp. 155–160.

⁷K. Lepage, "Bottom reverberation in shallow water: coherent properties as a function of bandwidth, waveguide characteristics, and scattering distributions," *J. Acoust. Soc. Am.* **106**, 3240–3254 (1999).

⁸H. Schmidt and J. Lee, "Physics of 3-D scattering from rippled seabeds and buried targets in shallow water," *J. Acoust. Soc. Am.* **105**, 1605–1617 (1999).

⁹K. V. Mackenzie, "Bottom reverberation for 530 and 1030 cps Sound I Deep Water," *J. Acoust. Soc. Am.* **33**, 1498–1504 (1961).

¹⁰T. C. Yang, "Scattering from boundary protuberances and reverberation imaging," *J. Acoust. Soc. Am.* **93**, 231–242 (1993).

¹¹N. C. Makris, "A spectral approach to 3-D object scattering in layered media applied to scattering from submerged spheres," *J. Acoust. Soc. Am.* **104**, 2105–2113 (1998); **106**, 518 (1999) (erratum).

¹²J. J. Bowman, T. B. A. Senior, and P. L. E. Uslenghi (Eds.), *Electromagnetic and Acoustic Scattering by Simple Shapes* (North-Holland, Amsterdam, 1969).

¹³F. B. Jensen, W. A. Kuperman, M. B. Porter, and H. Schmidt, *Computational Ocean Acoustics* (American Institute of Physics, New York, 1994).

¹⁴M. J. Lighthill, *An Introduction to Fourier Analysis and Generalized Functions* (Cambridge U. P., New York, 1980).

¹⁵N. C. Makris, "Active detection, classification and localization of fluctuating targets in shallow water," ASW Surveillance Programs FY99 Program Summaries (Office of Naval Research, 1999).

¹⁶P. Swerling, "Probability of detection for fluctuating targets," Rand Report RM-12-17 (1954); reissued in IRE Prof. Group Inf. Theory **IT-6**, 269–308 (1960).

¹⁷N. Levanon, *Radar Principles* (Wiley, New York, 1988).

¹⁸J. A. Ogilvy, *Theory of Wave Scattering from Random Rough Surfaces* (Hilger, New York, 1991).

¹⁹J. W. Goodman, *Statistical Optics* (Wiley, New York, 1985).

²⁰H. C. van de Hulst, *Light Scattering by Small Particles* (Dover, New York, 1981).

²¹N. C. Makris, "The effect of saturated transmission scintillation on ocean acoustic intensity measurements," *J. Acoust. Soc. Am.* **100**, 769–783 (1996).

²²R. J. Urlick, *Principles of Sound in the Sea* (McGraw-Hill, New York, 1983).

²³D. H. Berman, "Reverberation in waveguides with rough surfaces," *J. Acoust. Soc. Am.* **105**, 672–686 (1999).

²⁴M. Sundvik and P. Cable, personal communication.

²⁵N. C. Makris, Y. Lai, and P. Ratilal, "Measuring signal bearing, delay and time-frequency characteristics in a dispersive shallow-water waveguide," to be submitted to *J. Acoust. Soc. Am.*

²⁶N. C. Makris, C. S. Chia, and L. T. Fialkowski, "The bi-azimuthal scat-

- tering distribution of an abyssal hill,” J. Acoust. Soc. Am. **106**, 2491–2512 (1999).
- ²⁷N. C. Makris, “Imaging ocean-basin reverberation via inversion,” J. Acoust. Soc. Am. **94**, 983–993 (1993).
- ²⁸N. C. Makris, L. Z. Avelino, and R. Menis, “Deterministic reverberation from ocean ridges,” J. Acoust. Soc. Am. **97**, 3547–3574 (1995). [Bathymetry in Fig. 5 of this reference should be labeled <3600 m not <3200 m as shown. Also, the bistatic reverb for lfm s478 should be labeled >87 dB *re* 1 μ Pa in Fig. 24, not >80 dB *re* 1 μ Pa as shown.]
- ²⁹B. K. P. Horn and R. W. Sjoberg, “Calculating the reflectance map,” Appl. Opt. **18**, 1770–1779 (1979).
- ³⁰J. Moe and D. R. Jackson, “First-order perturbation solution for rough surface scattering cross section including the effects of gradients,” J. Acoust. Soc. Am. **96**, 1748–1754 (1994).
- ³¹Note $P_n^m(-z) = (-1)^n P_n^m(z)$ where z is the cosine between the incident and scattered wave directions. This should be used to convert Eqs. (8) and (9) of Ref. 11 from Ingenito’s definition to the standard one. In the former the object scatter function is defined in terms of the direction the incident wave comes from and in the latter it is defined in terms of the direction the incident goes to. It should be noted that in Ref. 11 Ingenito’s definition is used implicitly for all equations except Eqs. (16) and (17), where the standard definition is used.
- ³²J. A. Austin, Jr., C. S. Fulthorpe, G. S. Mountain, D. L. Orange, and M. E. Field, “Continental-margin seismic stratigraphy: assessing the preservation potential of heterogeneous geological processes operating on continental shelves and slopes,” Oceanography **9**, 173–176 (1996).
- ³³H. H. Essen, “Scattering from a rough sediment seafloor containing shear and layering,” J. Acoust. Soc. Am. **95**, 1299–1310 (1994).
- ³⁴D. Jackson, *APL-UW High Frequency Ocean Environmental Acoustic Models Handbook*, Chap IV, Bottom, APL-UW Technical Report TR9407 (Applied Physics Laboratory, Univ. of Washington, 1994).
- ³⁵P. M. Morse and K. U. Ingard, *Theoretical Acoustics* (Princeton U. P., Princeton, NJ, 1986), pp. 418–436.
- ³⁶A. V. Oppenheim R. W. Schafer, and J. R. Buck, *Discrete Time Signal Processing* (Prentice Hall, Englewood Cliffs, NJ, 1999).